NIST Technical Note 2068
Revision 1

Laboratory Tests of a Prototype Carbon Dioxide Ground-Source Air Conditioner

Harrison Skye
Wei Wu

This publication is available free of charge from:
https://doi.org/10.6028/NIST.TN.2068r1

National Institute of Standards and Technology
U.S. Department of Commerce

NIST Technical Note 2068
Revision 1

Laboratory Tests of a Prototype Carbon Dioxide Ground-Source Air Conditioner

Harrison Skye
Engineering Laboratory
National Institute of Standards and Technology

Wei Wu
School of Energy and Environment
City University of Hong Kong

This publication is available free of charge from:
https://doi.org/10.6028/NIST.TN.2068r1

April 2021

U.S. Department of Commerce
Gina M. Raimondo, Secretary

National Institute of Standards and Technology
James K. Olthoff, Performing the Non-Exclusive Functions and Duties of the Under Secretary of Commerce for Standards and Technology & Director, National Institute of Standards and Technology

National Institute of Standards and Technology Technical Note 2068 Revision 1
Natl. Inst. Stand. Technol. Tech. Note 2068 Rev. 1, 80 pages (April 2021)
CODEN: NTNOEF

This publication is available free of charge from:
https://doi.org/10.6028/NIST.TN.2068r1

Revision 1 notes

In Eqs. (4.8) and (4.9) on pg. 16, the denominator was changed to be divided, rather than multiplied, by η_{total}. The term later cancels out so no other text, graphs, results needed to be changed.

Old

$$\mathrm{COP}_{\mathrm{LLSL}} = \frac{Q_{\mathrm{evap,ref}}}{W_{\mathrm{com}}} = \frac{m_{\mathrm{ref}}\left(i_{10} - i_8\right)}{m_{\mathrm{ref}}\ \eta_{\mathrm{total}}\left(i\left(P_1, s_{13}\right) - i_{13}\right)} \tag{4.8}$$

$$\mathrm{COP}_{\mathrm{basic}} = \frac{Q_{\mathrm{evap,ref,basic}}}{W_{\mathrm{com,basic}}} = \frac{m_{\mathrm{ref,basic}}\left(i_{10} - i_5\right)}{m_{\mathrm{ref,basic}}\ \eta_{\mathrm{total}}\left(i\left(P_1, s_{10}\right) - i_{10}\right)} \tag{4.9}$$

New

$$\mathrm{COP}_{\mathrm{LLSL}} = \frac{Q_{\mathrm{evap,ref}}}{W_{\mathrm{com}}} = \frac{m_{\mathrm{ref}}\left(i_{10} - i_8\right)}{m_{\mathrm{ref}}\left(i\left(P_1, s_{13}\right) - i_{13}\right)/\eta_{\mathrm{total}}} \tag{4.8}$$

$$\mathrm{COP}_{\mathrm{basic}} = \frac{Q_{\mathrm{evap,ref,basic}}}{W_{\mathrm{com,basic}}} = \frac{m_{\mathrm{ref,basic}}\left(i_{10} - i_5\right)}{m_{\mathrm{ref,basic}}\left(i\left(P_1, s_{10}\right) - i_{10}\right)/\eta_{\mathrm{total}}} \tag{4.9}$$

Abstract

Environmental concerns are driving regulations to reduce the use of hydrofluorocarbons (HFCs) with high global warming potential (GWP) as refrigerants in heat pumps. CO_2 is an attractive alternative refrigerant because is it 'environmentally friendly' in terms of 'direct' emissions, with GWP = 1, and no ozone depletion potential (ODP). However, CO_2 heat pumps generally have a lower efficiency than HFC-based systems, and therefore have higher 'indirect' emissions, related to generating the electricity that powers them. The indirect emissions dwarf the direct emissions for most heating, air-conditioning and refrigeration applications, so it is critical for the equipment to operate with high efficiency. CO_2 air-source heat pumps (ASHPs) provide cooling with particularly low efficiency at high ambient temperatures where the CO_2 operates in a transcritical cycle. Using CO_2 in a ground-source heat pump (GSHP) offers the potential to overcome the low efficiency since a GSHP operates with lower heat-rejection temperature (for cooling), enabling the system to operate some of the time in a more-efficient subcritical cycle.

This report details the laboratory tests of a prototype residential liquid-to-air ground-source air conditioner (GSAC) using CO_2 as the refrigerant. The tests were performed in an environmental chamber and followed the ISO 13256-1 standard for rating GSHPs. The CO_2 GSAC operated either in a subcritical or a transcritical cycle, depending on the entering liquid temperature (ELT). The test results included the coefficient of performance (COP), capacity, sensible heat ratio (SHR), and pressures. The system incorporated a liquid-line/suction-line heat exchanger (LLSL-HX), which was estimated to cause a COP penalty of (0 to 2) % for ELTs ranging (10 to 25) °C, and benefit of (0 to 5) % for ELTs ranging (30 to 39) °C. The CO_2 system was compared to a 'low-cost', commercially-available R410A-based GSHP. With ELTs ranging (10 to 39) °C the CO_2 system cooling COP ranged (7.3 to 2.4), whereas the R410A system values ranged (6.1 to 3.2). At the 'standard' rating condition (ELT 25 °C), the CO_2 GSAC cooling COP was 4.14 and the R410A GSHP COP was 4.57. At 'part-load' conditions (ELT 20 °C) both systems had a COP of ≈4.92. Further effort is needed to increase the CO_2 system efficiency at ELTs greater than 20 °C, since it underperformed the R410A system in that temperature range.

Key words

Air conditioner, carbon dioxide, CO_2, ground-source heat pump, subcritical and transcritical cycles

Acknowledgements

The GSHP test apparatus was constructed by the National Institute of Standards and Technology (NIST) Heating, Ventilation, Air-conditioning, and Refrigeration (HVAC&R) Equipment Performance Group technicians, John Wamsley and Art Ellison. In addition to design and construction efforts, they performed critical maintenance and upgrades to the prototype CO_2 GSAC and the new test facility. John Wamsley assembled the refrigerant-, liquid-, and air-side components and instruments, and Art Ellison constructed the GSHX fluid-heating system and the associated safety circuit. Both technicians contributed to the data acquisition system. Vance Payne provided invaluable consultation on the test apparatus design and operation. Some of the tests reported here were diligently carried out by our summer undergraduate student from Penn State, Mike Bichnevicius. Optimized Thermal Systems (OTS), in Beltsville MD, designed and constructed the CO_2 GSAC; thanks to Paul Kalinowski, Dennis Nasuta, William Hoffman, and Cara Martin. OTS provided many additional details and insight about the unit after it was delivered to NIST. Thanks to Amanda Pertzborn, Piotr Domanski, Andy Persily, and the WERB board, for their reviews of this document that improved its technical and editorial quality. Also, thanks to Parham Elslam-Nejad at CanmetENERGY, École Polytechnique de Montréal, for his review and outside-NIST perspective.

Table of Contents

List of Figures

List of Tables

Nomenclature

Symbol	Units	Definition
A	m^2	Area
c	kJ / (kg·K)	Specific heat
C	--	Coefficient (e.g. airflow nozzle discharge coefficient)
COP	W / W	Coefficient of performance (thermal capacity per electricity input)
D	mm	Diameter
D	kg / m^3	Density measurement
Dew	°C	Dew-point measurement
DP	Pa	Differential pressure measurement
EER	Btu / (h·W)	Energy efficiency ratio (thermal capacity per electricity input)
ESP	Pa	External static pressure (pressure relative to ambient air pressure)
f	Hz	Compressor excitation frequency
H	mm	Height
i	kJ / kg	Specific enthalpy
k	--	Expanded uncertainty coverage factor ($k = 2$, 95 % confidence level)
L	mm	Length
m	kg / s	Mass flow
MF	kg / s	Mass flow measurement
N	--	Number
P	kPa, Pa; mm	Pressure; pitch
P	kPa, Pa	Pressure measurement
Q	W	Energy transfer
R	K / kW	Thermal resistance
Re	--	Reynolds number of air
RTD	°C	Resistance temperature detector measurement (platinum element)
s	kJ / (kg·K)	Specific entropy
SHR	W / W	Sensible heat ratio (sensible capacity divided by total capacity)
T	°C	Temperature
TC	°C	Thermocouple measurement

v	m^3/kg	Specific volume
v_{fan}	m^3_{ma}/kg_{da}	Specific volume of supply air, at fan exit (m^3 of moist air / kg of dry air)
v_n	m^3_{ma}/kg_{da}	Specific volume of air at the nozzle inlet (m^3 of moist air / kg of dry air)
v'_n	m^3_{ma}/kg_{ma}	Specific volume of air at the nozzle inlet (m^3 of moist air / kg of moist air)
V_d	m^3/s	Compressor volumetric displacement rate
V_{fan}	m^3_{ma}/s	Airflow rate at AHU fan
V_n	m^3_{ma}/s	Airflow rate at nozzle
V_{pump}	m^3/s	Liquid flow rate through HTF pump
w	mm	Width
W	W	Electrical power
W	W	Electrical power measurement
Wh	W·h	Cumulative electrical energy measurement
x	--	Vapor quality (vapor mass fraction of two-phase fluid)

Greek Symbol	**Units**	**Definition**
γ	--	Heat loss ratio (fraction of work input to a component that is dissipated as heat to the ambient air)
δ	mm	Thickness
Δ	--	Difference
ε	--	Effectiveness of a heat exchanger
η	--	Efficiency
μ	kg/(m·s)	Dynamic viscosity
ω	kg_w / kg_{da}	Air humidity ratio (kg of water vapor / kg of dry air)

Subscript	**Definition**
adj	For all: adjustment to the electricity input to only include the amount needed to move air (fan) or HTF (pump) through the GSHP, per ISO 13256-1 For COP: adjusted fan heat input, and adjusted fan & pump electricity For *Q*: adjusted fan heat input For SHR: GSAC adjusted sensible capacity divided by adjusted total capacity For *W*: adjusted fan & pump electricity
air	Air or air-side
b	Bore of compressor cylinder
basic	Basic cycle without LLSL-HX
com	Compressor
cond	Condenser/gas-cooler
correction	Correction to the electricity input to only include the amount needed to move air (fan) or HTF (pump) through the GSHP, per ISO 13256-1
crit	Critical point
cyl	Compressor cylinders
d	Discharge, nozzle discharge, displacement
da	Dry air (i.e. considering only portion of air without moisture)
evap	Evaporator
ext	External static pressure
f	Fin
fan	Fan (i.e. blower)
fg	Latent heat of vaporization
i	Inside diameter
imb	Imbalance of energy transfer measurements
in	Inlet
l	Longitudinal tube pitch
lat	Latent cooling capacity (i.e. energy related to condensing water vapor out of air)
liq	Liquid (HTF), or, section of heat exchanger filled with liquid refrigerant
LLSL	Liquid-line/suction-line heat exchanger, or cycle containing a LLSL-HX
ma	Moist air (i.e. considering mixture of air and water vapor)
max	Maximum

n	Nozzle For D and A: nozzle throat For μ: nozzle inlet
o	Outside diameter
out	Outlet
p	Plate (of a plate heat exchanger), length/area of fluid flow in brazed-plate heat exchanger, or constant-pressure
pinch	Pinch point (location of minimum temperature difference in a heat exchanger)
pump	Pump
ref	Refrigerant, refrigerant flow for the cycle that includes a LLSL-HX
return	Return duct, i.e. the air inlet of the GSAC
s	Compressor stroke
sens	Sensible cooling capacity (i.e. energy related to changing the air temperature)
SupCrit	Supercritical
supply	Supply duct, i.e. the air outlet of the GSAC
sys	Entire GSAC system
t	Transverse tube pitch
total	Total For Q: sum of sensible and latent capacities For W: sum of electricity input to compressor, fan, and pump
v	Volumetric (e.g. compressor volumetric efficiency)
vap	Section of heat exchanger filled with vapor refrigerant
w	Water, water vapor, fin wave (pitch or height)
1 to 13	Refrigerant thermodynamic states as defined in Fig. 5
2ph	Section of heat exchanger filled with 2-phase refrigerant

Abbreviation	**Definition**
AHRI	Air-conditioning, Heating, and Refrigeration Institute
AHU	Air-handling unit
AMCA	Air Movement and Control Association
ANSI	American National Standards Institute
ASHP	Air-source heat pump
ASHRAE	American Soc. of Heating, Refrigeration, and Air-conditioning Eng.
BD-H	Burst disc: high-pressure
BD-L	Burst disc: low-pressure
CFC	Chlorofluorocarbon
CFM	Cubic feet per minute
CFR	Code of Federal Regulations (U.S.)
CI	Confidence interval
CO_2	Carbon dioxide
DAQ	Data acquisition
DGX-GSHP	Direct ground-exchange ground-source heat pump
DOE	Department of Energy (U.S.)
EEV	Electronic expansion valve
ELT	Entering liquid temperature (entering the GSAC or GSHP from the GSHX)
EPDM	Ethylene-propylene-diene (rubber)
GPM	Gallons per minute
GSAC	Ground-source air conditioner
GSHP	Ground-source heat pump
GSHX	Ground-source heat exchanger
GWP	Global warming potential
HCFC	Hydrochlorofluorocarbon
HFC	Hydrofluorocarbon
HFO	Hydrofluoroolefin
HPWH	Heat pump water heater
HSPF	Heating seasonal performance factor
HTF	Heat transfer fluid
HVAC&R	Heating, ventilation, air-conditioning, and refrigeration
ID	Inner diameter

IHX	Internal heat exchanger (i.e. LLSL-HX)
ISO	International Standards Organization
LLSL-HX	Liquid-line/suction-line heat exchanger (i.e. internal heat exchanger)
MAWP	Maximum allowable working pressure
MD	Maryland (USA)
NIST	National Institute of Standards and Technology (United States)
NPT	National Pipe Thread
OD	Outer diameter
ODP	Ozone depletion potential
OTS	Optimized Thermal Systems (contractor who built the GSAC)
PHX	Plate heat exchanger
PID	Proportional-integral-derivative controller
PS-H	Pressure switch: high-pressure activated
PS-L	Pressure switch: low-pressure activated
PVC	Polyvinyl chloride plastic
R12	Refrigerant dichlorodifluoromethane
R125	Refrigerant pentafluoroethane
R134a	Refrigerant 1,1,1,2-tetrafluoroethane
R22	Refrigerant difluoromonochloromethane
R407C	Refrigerant mixture: R32/125/134a, 23/25/52 % by mass
R410A	Refrigerant mixture: R32/125, 50/50 % by mass
REFPROP	Reference fluid thermodynamic and transport properties database (NIST)
RPM	Revolutions per minute (compressor)
RTD	Resistance temperature detector (platinum)
SCR	Silicon controlled rectifier (variable power supply)
SINTEF	Stiftelsen for industriell og teknisk forskningn (Trondheim, Norway)
SHR	Sensible heat ratio
TLC	Temperature limit controller
UV	Ultra-violet
VCR	Variable-compression ratio (a type of tube fitting that uses a metal gasket)

1 Introduction

1.1 Background and literature review

The use of CO_2 (carbon dioxide) in refrigeration dates back to 1866 when Thaddeus Lowe, in Texas, U.S., adapted a hydrogen compressor for use with CO_2 and used it for manufacturing artificial ice. Franz Windhausen patented an improved CO_2 compressor, which was further enhanced by Everard Hesketh in 1889; the J&E Hall company installed over 400 refrigeration systems using these compressors [1]. CO_2 was less efficient and more expensive than ammonia-based refrigeration, but it was preferred for marine transport because CO_2 was much safer than the toxic and flammable ammonia. However, ammonia took back market share in the early 20th century because: (1) its safety record improved thanks to electrically-welded joints, and (2) it had far superior efficiency (compared to CO_2) for tropical climates. The advent of chlorofluorocarbon (CFC) refrigerants (first patented in 1931 by Thomas Midgley Jr. [2]) and hydrochlorofluorocarbon (HCFC) refrigerants revolutionized the heating, ventilation, air-conditioning, and refrigeration (HVAC&R) industry, as these working fluids had the safety characteristics of CO_2 (non-flammable, non-toxic) and efficiency approaching ammonia. Subsequently, the use of CO_2 sharply dropped between the 1950s and the 1970s [1].

However, when CFCs and HCFCs are inadvertently released into the atmosphere (i.e. 'direct emissions') they cause stratospheric ozone depletion. The refrigerants release chlorine when exposed to the intense ultra-violet (UV) light in the atmosphere, and the chlorine acts as a catalyst in a chemical reaction that consumes ozone. So in 1987, the Montreal Protocol was adopted to restrict and eventually eliminate the use of CFCs and HCFCs. The chlorine-free replacements, hydrofluorocarbons (HFCs), also have an environmental problem of high global warming potential (GWP), with 100-year GWP values hundreds to thousands of times larger than that of CO_2 ([3], p. 732). The GWP is a measure of how well a substance traps long-wave radiation emitted from the earth's surface relative to an equal mass of CO_2 over a specified time horizon (commonly 100 years). Concerns about the environmental impacts of global climate change are driving efforts to limit emissions of high-GWP substances. In the European Union the F-gas regulation [4] mandates that by the year 2030, the total GWP of manufactured/imported HFCs must be phased down to 21 % of the average levels from the years 2009 through 2012. The Kigali Amendment to the Montreal Protocol [5] requires the participating parties to gradually reduce HFC use by (80 to 85) % by the late 2040s.

Major efforts are underway to identify alternative refrigerants with a lower GWP. Chemical manufacturers are producing halogenated olefins (e.g., hydrofluoroolefins (HFOs)), which are a special subset of HFCs that feature unsaturated bonds. These bonds remain intact while the fluid is inside the equipment but dissociate quickly when exposed to the atmosphere, so HFOs have a short atmospheric lifetime and correspondingly a low GWP. However, the unsaturated bonds can cause an increase in flammability, and all HFOs that could potentially be used in small unitary heat pumps (primarily R1234yf and R1234ze(E)) have a flammability rating of '2L' [6] (lower flammability with a burning velocity ≤ 10 cm/s) or higher [7], [8]. The Air-Conditioning, Heating, and Refrigeration Institute (AHRI) led a collaborative effort to evaluate the drop-in and soft-optimized performance of low-GWP alternatives largely consisting of HFOs and HFO/HFC blends [9].

CO_2 is an attractive refrigerant to mitigate the global warming effect of direct emissions since it has a very low GWP (GWP = 1) and no ozone depletion potential (ODP = 0). Additionally, it has a safety classification of A1 (non-toxic, non-flammable, [6]), and is inexpensive. A primary barrier to widespread use of CO_2 is that for many applications, the cycle efficiency of CO_2 is low compared to HFC-based systems. CO_2 has a low critical temperature (T_{crit} = 30.98 °C, P_{crit} = 7377 kPa, [10]), so many CO_2 systems operate in a subcritical cycle near the critical point, or in a transcritical cycle where the high-pressure side operates above the critical point and the low-pressure side operates below the critical point. The efficiency of a basic refrigeration cycle is low near and/or above the critical point of the refrigerant. This low efficiency results in higher emissions from the power plant generating the electricity to operate the equipment, and these emissions essentially comprise the 'indirect' emissions (there are also minute contributions from equipment manufacturing and disposal) for typical HVAC&R equipment [11]. Lee et al. [11] showed that the indirect emissions comprised ≈90 % of the total lifetime emissions (sum of direct and indirect) for a R410A (GWP = 1924, ([3], p. 732)) air-source heat pump (ASHP). Since CO_2 has a GWP = 1 the direct emissions are essentially negligible, so only the indirect emissions are significant. Consequently, to achieve a reduction in total lifetime emissions, the CO_2 system must be more than 90 % as efficient as a R410A system. The Lee et al. study [11] also showed that using an HFO/HFC blend could reduce the total lifetime emissions by ≈(4 to 7) % compared to a R410A system. To achieve similar total lifetime emissions, the CO_2 system would need to be ≈(94 to 97) % as efficient as a R410A system.

An engineering challenge to using CO_2 is the high operating pressures. For example, at a condenser saturation temperature of 30 °C, the approximate saturation pressure for CO_2 is 7200 kPa compared to 1900 kPa for R410A. R410A is itself considered a high-pressure fluid, so designing a heat pump to work at the even higher pressures of CO_2 is a significant challenge. However, in some respects, the high operating pressures of CO_2 can be advantageous since the density is correspondingly high. With the high-density CO_2, for a given mass flow and flow-passage size, the velocity and corresponding frictional pressure drop is relatively small. Therefore, tube diameters can be (60 to 70) % smaller with CO_2 [12], which reduces the tube wall thickness needed to withstand the higher pressures. Heat exchangers can be manufactured with more air-side heat transfer area since the smaller refrigerant tubes occupy less space. Finally, the compressor displacement required to achieve a target capacity is significantly reduced with the high-density suction gas, so even though the walls are heavier, the overall size of CO_2 compressors can be similar to that of HFC compressors [12].

Gustav Lorentzen is credited with breathing new life into CO_2 as a refrigerant in the 1990s with proposals for applications where CO_2 could potentially compete with CFCs, HCFCs, and HFCs [13]. In particular, he argued the temperature glide of supercritical CO_2 in the gas cooler made the cycle ideal for water heating. The CO_2 temperature glide could be matched to the water temperature change in a counterflow heat exchanger for efficient heat transfer. This idea was further explored by Stene [14], who compared the energy use of a hybrid space-heating/water-heating system using CO_2 to systems using HFCs (R410A or R407C). Stene found the CO_2 system was more efficient for water heating, but less efficient for space heating. The CO_2 system met the combined load (space heating and water heating) using less energy if the water heating comprised 25 % or more of the heating load. The 25 % fraction was reasonable for highly-efficient homes but too high for traditional homes. Hwang and Radermacher [15] used a simulation to show that an optimized CO_2 heat pump water heater (HPWH) could be up to 11 % more efficient than a similar R22 system.

The environmental benignity of CO_2 makes it attractive for automotive air conditioners where refrigerant leakage tends to be large. Gustav Lorentzen [16] received a seminal patent for an automotive CO_2 air conditioner featuring a liquid-line/suction-line heat exchanger (LLSL-HX, i.e. internal heat exchanger, IHX), and a receiver at the exit of the evaporator. This system achieved Coefficients of Performance (COPs) that were (100 to 138) % of those for a similar R12-based air conditioner. Interestingly, a simple theoretical model predicted the CO_2 system would have a COP that was *less* than the R12 system by 50 %. However, there were three important effects not captured by the model that improved the relative performance of CO_2 when applied to hardware. The effects included:

1) The CO_2 system had superior evaporator heat transfer due to higher refrigerant-side heat-transfer coefficients, absence of a superheat zone towards the outlet, and larger air-side heat transfer area and lower air-side pressure drop enabled by smaller tubes.

2) The CO_2 system gas-cooler outlet temperature had a closer approach to the ambient air temperature than the R12 system had at the condenser outlet.

3) The CO_2 compressor isentropic efficiency was ≈70 %, considerably higher than the R12 value of ≈50 %. The difference was attributed to lower compression ratios with CO_2, 2.5 to 3.5, compared to the R12 values of 5 to 7.

This system was adopted a few years later in the European 'Refrigeration and Automotive Climate systems under Environmental Aspects' (RACE) project [17], in which researchers and car manufactures worked together to develop and test a mobile CO_2 air conditioner. The results were promising as the CO_2 system could achieve comparable efficiency to the benchmark conventional R134a system, and for some conditions the CO_2 system had up to 40 % higher efficiency. However, Brown et al. [18] noted that while the CO_2 and R134a systems used heat exchangers constrained to the same volume and face area, the CO_2 system used microchannel heat exchangers that had substantially more surface area than the fin-tube heat exchangers employed by the R134a system. The Brown et al. [18] simulation showed the R134a system could achieve (29 to 60) % higher COP than the CO_2 system when the heat exchanger air-side heat transfer areas were the same and the refrigerant circuitries were optimized.

CO_2 systems generally have lower efficiency than HCFC- or HFC-based systems for space cooling but can have higher efficiency for space heating. The previously mentioned Hwang and Radermacher study [15] showed that the CO_2 system had 7 % lower COP than the R22 system for delivering chilled water. Peter Neska summarized test results from SINTEF (research institution in Trondheim, Norway) showing that a CO_2 ASHP had slightly lower cooling, but higher heating efficiency [19], [20]. Further, the CO_2 system could maintain a higher heating capacity at low ambient temperatures, reducing dependence on auxiliary heat (usually an electric resistance heater with a COP of 1). Considering the reduced auxiliary heat, the CO_2 system achieved a 20 % higher heating seasonal performance factor (HSPF) than the R22 system. Jin et al. [21] showed a more unfavorable result for CO_2 heat pumps applied in the cooling-dominated city of Shanghai, China. The seasonal COP for a CO_2 ASHP was 2.52 compared to 4.17 for a similar R410A system. Even the CO_2 ground-source heat pump (GSHP) only had a COP of 2.87, and the hybrid system using a GSHP with a supplemental air cooler achieved a COP of 3.55. Jakobsen et al. [22] compared experimental data for a R410A ASHP with simulation studies for a similar CO_2 system and predicted the CO_2 system had a (1 to 2) % higher cooling COP and a (38 to 41) % higher heating COP. In a study similar to the one mentioned in the preceding paragraph for automotive air conditioners, Brown et al. [23] noted that some studies unfairly advantaged CO_2 with advanced microchannel heat exchangers, while the compared 'conventional' R22 and R410A systems used finned-tube heat exchangers with smaller surface area. Brown et al. [23] used a simulation to compare CO_2 and R22 air conditioners with microchannel flattened-tube heat exchangers constrained to the same air-side heat transfer area and found the COP with CO_2 was lower by (42 to 57) %.

There have been many efforts to improve the efficiency of CO_2-based systems by changing the underlying cycle. Many studies focus on reducing the relatively large throttling losses for CO_2 systems by replacing the isenthalpic expansion device or using a LLSL-HX. Robinson et al. [24] showed that replacing the expansion valve with a turbine expander, with a 60 % isentropic efficiency, reduced the cycle irreversibility by 33 %. A 100 % efficient LLSL-HX increased cycle COP by 7 % when used with an expansion valve, but decreased COP by 8 % when paired with the expander with 60 % isentropic efficiency. In a study for automotive applications, Boewe et al. [25] showed the LLSL-HX increased capacity by 11 %, increased COP by 23 %, and reduced the difference between the pressures that respectively maximized the COP and capacity. Similar to expanders, ejectors reduce throttling losses, but without any moving parts. Li et al. [26] showed a 16 % improvement in COP with an ejector, compared to the basic cycle. Shet et al. [27] studied CO_2 performance in cycles with different configurations including: a basic cycle with an expansion valve (COP 1.84), an expansion valve plus a LLSL-HX (COP 1.87), a vortex tube expander (COP 1.89), and a turbine expander (COP 2.31). The high-side pressure for transcritical cycles can be controlled to achieve maximum COP or capacity. This control is achieved, for example, using the expansion valve to regulate the high-side pressure rather than the superheat [12], [16], [28]. Alternatively, the refrigerant charge can be adjusted. Cho et al. [29] showed that as the CO_2 charge was increased the COP quickly reached a maximum, then slowly decreased, whereas the capacity continued to increase after the maximum COP point. The performance of the CO_2 system was more sensitive to the charge than HFC-based systems.

The efficiency of heat pumps decreases with temperature lift, so ASHP performance degrades with higher outdoor air temperatures. The outdoor air temperature regularly reaches (30 to 35) °C or higher in cooling mode, so condenser saturation temperatures of (35 to 40) °C or higher are common. The performance of CO_2 ASHPs is particularly poor at these air temperatures since the system operates in a transcritical cycle. Ground-source heat pumps (GSHPs) are potentially a better use for CO_2 since the operating condenser/gas-cooler temperatures in the cooling mode are lower. GSHPs reject energy to (and extract energy from) a ground-source heat exchanger (GSHX), and the ground temperatures are more favorable than the outdoor air temperatures; therefore, the operating efficiency of GSHPs tend to be higher than ASHPs. For example, in Gaithersburg, MD, U.S., the average ground temperature is about 14 °C, but the summer air temperatures regularly exceeds 30 °C [30]. With a properly-sized GSHX, the GSHP entering liquid temperature (ELT) of the heat-transfer fluid (HTF) exchanging heat with the ground will generally be much lower than the outdoor air temperature (for cooling), though the ELT can reach (30 to 35) °C late in the cooling season ([31], Ch. 35 'Geothermal Energy', p 35.25). Therefore, a CO_2-based GSHP can operate with lower pressures and higher efficiencies than a CO_2 ASHP, and the CO_2 GSHP may be competitive with GSHPs that use R410A.

There are relatively few studies in the open literature showing performance of CO_2 GSHPs. A 2006 patent by Kunio Hamanaka [32] details a CO_2 GSHP that uses groundwater as a heat source, and provides simultaneous refrigeration as well as water heating to 90 °C. Jiang et al. [33] constructed a prototype CO_2 GSHP that provided heating, cooling, and hot water. In heating mode, the COP was about 3.0. Several researchers studied direct-ground-exchange GSHPs (DGX-GSHPs) where the refrigerant circulates in the GSHX, rather than a secondary HTF [34]–[37]. Jin et al. [38] considered a hybrid system to increase the cooling efficiency, where the refrigerant rejected heat in an air cooler before it was further cooled by the HTF circulating in the GSHX. This configuration reduced the fraction of the heat rejection borne by the GSHX and therefore kept the ELT low, which in turn increased the GSHP efficiency.

The goal of this study was to provide experimental data useful for assessing the merits of CO_2-based GSHPs. This report shows performance measurements of a prototype residential liquid-to-air CO_2 ground-source air conditioner (GSAC). The system was designed to only provide cooling, to simplify the construction and testing. Key information about system efficiency, capacity, and operating pressures were recorded. An estimation of the COP benefit/penalty of including a LLSL-HX was performed. Lastly, to gauge the CO_2 GSAC against the current market, the test data were compared with manufacturer's data for a commercially-available R410A-based GSHP.

1.2 Report overview

The tested prototype GSAC cools the indoor air while rejecting heat to the HTF that would circulate in the GSHX (Fig. 1, Fig. 2). The system implements a basic vapor-compression cycle with a LLSL-HX, where the LLSL-HX increases the specific refrigeration capacity by lowering the refrigerant enthalpy after the condenser/gas-cooler (condenser in subcritical mode, gas cooler in transcritical mode) before it goes to the expansion valve. The GSAC was tested in an environmental chamber according to International Standards Organization (ISO) standard 13256-1 [39], for rating liquid-to-air heat pumps. A chiller emulated the heat dissipation in the GSHX and regulated (in combination with a trim heater) the ELT of the HTF. The four primary test conditions from the ISO standard included the: 'standard' (ELT 25 °C), 'part-load' (ELT 20 °C), 'minimum' (ELT 10 °C), and 'maximum' (ELT 39 °C, Section 3.4.1 explains why 40 °C from ISO 13256-1 was not used) conditions. In addition, the unit was tested at five more ELTs that ranged (10 to 36.8) °C, and a repeated 'standard' test, for a total of ten tests. Depending on the ELT, the system operated either with a subcritical or transcritical cycle.

Section 2 details the GSAC design and Section 3 shows the test facility. Section 4 describes the data reduction methods and Section 5 discusses the results including a comparison of the CO_2 GSAC data with manufacturer's data [40] for a commercially-available R410A GSHP in terms of: COP, capacity, sensible heat ratio (SHR), and pressures. Section 6 summarizes the results and recommendations for future work.

Key results shown in Section 5 include:

- **CO_2 GSAC vs. R410 GSHP (Fig. 12):** With ELTs ranging (10 to 39) °C the CO_2 system cooling COP ranged (7.3 to 2.4), whereas the R410A system values ranged (6.1 to 3.2). At the 'standard' rating condition (ELT 25 °C), the CO_2 GSAC cooling COP was 4.14 and the R410A GSHP COP was 4.57, per the manufacturers data sheet [40]. Both systems exceeded the minimum cooling COP of 3.8 required by the Department of Energy (DOE) [41] for GSHPs sold in the U.S., but neither system achieved the minimum cooling COP of 5.0 for an 'Energy Star' rating [42]. At the 'part-load' conditions (ELT 20 °C) the CO_2 system had a COP of 4.92, which nominally equaled the R410A GSHP value. At lower ELTs ('ELT-1,2'), (10 to 15) °C, the CO_2 GSAC had higher COP and total capacity than the R410A system; at higher ELTs ('ELT-3,4,5' and 'maximum'), (30 to 39) °C, the R410A system had higher values. The CO_2 system had a higher SHR across the entire ELT range, and therefore removed less moisture from the air. For the 'standard' and 'part-load' conditions the CO_2 GSAC SHRs were 0.80 and 0.78, respectively; for the R410A GSHP they were 0.72 and 0.71.
- **Pressures (Fig. 13):** For the CO_2 GSAC, the maximum high-side and low-side pressures were 9500 kPa and 5500 kPa, respectively.
- **LLSL-HX (Fig. 21):** For the CO_2 GSAC, the LLSL-HX was estimated to have caused a COP penalty of about (1 to 2) % for ELTs ranging (10 to 25) °C, and a benefit of (0 to 5) % for ELTs ranging (30 to 39) °C. The estimation compared the measurements of the CO_2 GSAC with the LLSL-HX to predicted cycle performance without the LLSL-HX.

2 CO_2 Ground-Source Air Conditioner Design & Construction

The tested prototype residential liquid-to-air CO_2 GSAC (Fig. 2) has a nominal cooling capacity of 7 kW (2 tons) [43]. The refrigerant circuit consists of an inverter-driven semi-hermetic reciprocating compressor, a fin-tube evaporator (A-frame; fins have a sine-wave enhancement; tubes have rifled inner surface), a plate heat exchanger (PHX) condenser/gas-cooler, a smaller PHX LLSL-HX, an electronic expansion valve (EEV), and an accumulator. A superheat controller adjusts the EEV position to regulate the evaporator-outlet superheat. Both PHXs have chevron-enhanced surfaces on both sides of the plates. The system also includes a fan (i.e. blower) and a GSHX pump.

The system operates in either a subcritical or transcritical cycle depending on the ELT. The larger PHX functions as a condenser in a subcritical cycle when the ELT is low (25 °C or below for the tests here), and the CO_2 can reject heat through condensation. When the ELT is high the PHX operates as a gas cooler in a transcritical cycle since the high-side pressure is above the CO_2 critical point. The LLSL-HX reduces the refrigerant enthalpy after the condenser (and therefore at the evaporator inlet), and therefore increases the capacity per unit mass flow. The penalty of including the LLSL-HX in the cycle is a higher compressor suction and discharge temperatures, lower suction density and therefore lower volumetric cooling capacity, and higher compressor work per unit of mass flow. The accumulator protects the compressor suction from any inadvertent liquid carryover leaving the LLSL-HX.

The specifications of the main components are presented in Table 1. Further component details are given in subsequent tables and figures, including the semi-hermetic reciprocating compressor (Table 2), the A-frame fin-tube heat exchanger (Fig. 3, Fig. 4, and Table 3), the PHXs (Fig. 3, Table 4), and the connecting tubes and auxiliary components (Table 5). The volumes of the connecting tubes and auxiliary components are important because they affect the amount of refrigerant in the system.

The unit components were attached to an aluminum frame (Fig. 2 (a)). The commercially-available air handling unit (AHU) was modified by installing the evaporator (Fig. 2 (b)), which was specially constructed using small-diameter, heavy-walled tubes, to withstand the high operating pressures of CO_2. The tubing between the refrigeration components was made of high-strength $CuFe_2F$ alloy (2 % iron) [44], and the tube connections were brazed with a high-strength alloy. Where separable connections were required, variable-compression-ratio (VCR) tube fittings were used. The VCR fittings utilize a crushable metal gasket and are less prone to leaks than other separable fittings. Threaded fittings were avoided to minimize the potential for leaks; the compressor fittings were threaded but all other connections were either brazed or used VCR fittings.

The high operating pressures were a major design consideration; the high-pressure side components (between the compressor discharge and the EEV inlet) all have a maximum allowable working pressure (MAWP) of at least 12 000 kPa, and the low-pressure side components (between the EEV outlet and compressor suction) have a MAWP of at least 7000 kPa (Table 1). A pressure switch (PS-H in Fig. 5) turns the compressor off if the discharge pressure rises above 10 800 kPa. Furthermore, the system is protected by burst discs on the high- and low-pressure sides, respectively 13 900 kPa and 7000 kPa (BD-H, BD-L, in Fig. 5). The system could not withstand prolonged exposure to temperatures near or greater than 28.7 °C when it was off, since the associated CO_2 saturation pressure equals the low-pressure burst disc limit (7000 kPa). A future commercially-produced system would need to be designed to withstand higher pressures, since the system will certainly be exposed to higher temperatures during use (e.g. if the indoor temperature were high because the cooling equipment was off) or during transportation from the manufacturer to the end-user.

The GSAC includes a few other safety controls (Fig. 5). A low-pressure switch turns off the GSAC if the suction pressure drops below 2170 kPa (PS-L in Fig. 5). Additionally, the compressor does not turn on unless the flow switch (FS in Fig. 5) detects more than 3.8 L/min of HTF through the GSAC.

3 Test Apparatus

The GSAC test apparatus was used to quantify the thermal and electrical energy transfers in the system, which in turn were used to determine the salient performance metrics of capacity, COP, and SHR. The instruments and their uncertainties are listed in Table 6, all uncertainties were smaller than the values required by ISO 13256-1 [39]. The GSAC was tested in a large environmental chamber that controlled the air dry-bulb and dew-point temperatures entering the GSAC return and surrounding the GSAC (Fig. 6). A flow of temperature-controlled HTF liquid was provided to the GSAC to emulate the flow from a GSHX; the temperature was controlled using a chiller and a circulation (trim) heater.

All reported measurements are the average of a 120-sample steady-state window with a period of 15 s (30 min sample window), recorded using an electronic data acquisition (DAQ) system. Steady-state criteria used (though not given by the ISO standard) included: all sensor readings varying non-monotonically in the sample window (particularly, the compressor discharge temperature, which always required the most time), a stable sample window standard deviation, and a stable energy balance on the condenser/gas-cooler and evaporator.

3.1 Refrigerant-side measurements

Refrigerant-side measurements (Fig. 5) were used to characterize the thermodynamic states of the CO_2 in the GSAC, numbered 1 to 13. Temperatures were measured with thermocouples soldered to the tube surfaces (TC 1100 to TC 1109). Pressure transducers were attached to the refrigeration lines using VCR connections (P 1200 to P 1216). A coriolis meter (with VCR fittings) in the liquid line after the LLSL-HX measured the mass flow rate (MF 1400) and density (D 1500). The compressor electric power (W 1304) and total energy input (Wh 1404) were measured between the inverter and the compressor.

3.2 Air-side measurements and components

The primary capacity measurement was on the air side. Temperatures were measured using in-stream air-RTD probes; differential and external static pressures (ESP) were measured using pressure transducers; air moisture content was measured using chilled-mirror dew-point transmitters; and airflow was measured using a nozzle (Fig. 5, Fig. 7, Fig. 9, Fig. 10). The GSAC fan power and total energy input were respectively measured using W 1306 and Wh 1406 (Fig. 5).

The conditioned air from the environmental chamber was drawn into the GSAC by the AHU fan, and then cooled by the GSAC. After the GSAC supply (Fig. 7), the air moved through a straight 1220 mm section, a u-bend, a 90° bend, a mixer and straightener, a 'nozzle airflow measuring apparatus', and finally exited the booster fan back into the environmental chamber. The nozzle airflow measuring apparatus was an enlarged section of the duct that included the nozzle, as well as diffusion baffles before and after the nozzle, per ISO 13256-1.

Temperature measurements for each location (e.g. return, supply, and after the mixer) were the average readings from three RTDs placed at the centers of equal rectangular cross-section areas of the duct (Fig. 8(a)). The RTDs were mounted using compression tube fittings threaded into aluminum plates, which in turn were fastened to the duct with screws, and the plates were sealed with caulk ((Fig. 8(b, c)). The GSAC return-air temperature was the average of RTDs 3700, 3701, and 3702. A common household box fan was used to mix the return air entering the GSAC to minimize stratification. The GSAC supply-air temperature was the average of RTDs 3703, 3704, and 3705. The RTDs after the mixer (RTDs 3706, 3707, and 3607) were used to compute the air properties needed for calculating airflow rate through the nozzles.

As an aside, some heat pump test standards (e.g., ANSI/ASHRAE 37 [45]) require the supply-air temperature measurement to occur after the mixer (e.g., RTDs 3706, 3707, and 3607), though the ISO 13256-1 standard does not have this requirement. Mixing was unnecessary here since the GSAC fan mixed the air very well and the maximum difference between the readings from RTDs 3703, 3704, and 3705 was typically less than 0.1 °C, so these sensors were used to measure the supply-air temperature. These sensors were closer to the GSAC supply and therefore the impact of duct heat leak on the supply-air temperature measurement was minimized; this in turn yielded a better sensible capacity measurement. If instead, RTDs 3706, 3707, and 3607 had been used, the associated duct heat leak would have resulted in an additional (1 to 1.5) % error in the capacity measurement.

Chilled-mirror dew-point transmitters measured the return- and supply-air moisture content (Fig. 5, Fig. 7) and were subsequently used to determine the latent capacity. The return sensor (Dew 3504) was in the center of the GSAC return duct opening and was covered by a sintered screen (provided by the manufacturer) to minimize contamination from dust. The supply sensor (Dew 3506) measured an air sample drawn out of the duct by a ‘sampling module’ (Table 7), at 0.025 L/s (less than 0.01 % of bulk airflow), from a PVC plastic sample tree located in the duct after the mixer and straightener.

The air pressure was measured using piezometer rings (Fig. 8(d)) to effectively average the pressure from the four sides of the duct. The pressure taps measured static pressure and consisted of barbed fittings threaded into aluminum plates ((Fig. 8(b, c)), similar to the RTD aluminum plates. Each tap was located at the center of each side of the duct, and they were connected using 6 mm ID tubing to form the piezometer ring. The external static pressure measurements included the GSAC supply-air ESP (DP 3319) and the nozzle-inlet ESP (DP 3322). The GSAC return ESP was not measured and was considered to be 0 Pa because there was no return duct. The nozzle pressure difference was measured by DP 3320, and DP 3321 served as a secondary sensor.

The airflow was measured using a nozzle embedded in a ‘nozzle board’ fabricated from a 19-mm-thick sheet of smooth plywood (Fig. 9, Fig. 10, Table 8). The nozzle board was located inside the nozzle airflow measuring apparatus. The pressure difference across the nozzles (DP 3320) along with the temperature measurement after the mixer (RTDs 3706, 3707, and 3607) were used to compute the air properties and the airflow, which ranged (343 to 352) L/s.

The nozzle board has four nozzles, though only nozzle #4, with a throat diameter of 126.87 mm, was used for these tests. For future tests requiring a greater range of flow (e.g. for variable-speed GSHPs), the four nozzles in combination can measure a flow of (90 to 770) L/s, while maintaining a throat velocity of (15 to 35) m/s as required by ISO 13256-1 ([39], p. 30), and with a minimum nozzle pressure drop of 250 Pa to stay in the top 2/3 of the differential pressure transducer range (DP 3320). Distances between the nozzles, and between the nozzles and the duct walls, were selected to follow the requirements of ISO 13256-1. Nozzles not being used were covered with the nozzle manufacturer's aluminum cap and sealed with painter's tape. The tightness of the seal on the unused nozzles was verified by seeding glycerin particles (i.e. from a 'fog machine') into a flow of air through the duct, and visually confirming no air leakage. The nozzles were manufactured according to the ASNI/AMCA 210-16 (ANSI/ASHRAE 51-16) standard [46]. The throat length, as specified by [46], was 0.6 times the nozzle diameter. This is slightly different from the ISO 13256-1 standard [39], which specified a throat length of 0.66 times the nozzle diameter. All other nozzle dimensions are identical in the two standards.

The nozzle throats passed through clearance holes cut into the nozzle board using a jigsaw (Fig. 10). Each nozzle base rested in a counterbore in the nozzle board, cut using a router, to a depth matching the thickness of the nozzles (3.2 mm), so the bottoms of the nozzle bases were flush with the board. The counterbores extended from the clearance hole to a diameter slightly larger than the nozzle base. The board was sanded smooth after the cutting processes, to minimize turbulence. Finally, the nozzles were set into the counterbores and sealed with silicon caulk.

Parasitic heat leak and airflow leak to/from the duct were controlled to minimize their distortion of temperature and flow measurements. The duct was insulated between the GSAC and the temperature measurement before the nozzle airflow measuring apparatus (Fig. 6), with 76 mm of foil-faced fiberglass (R-value 1.46 $m^2 \cdot K/W$). The duct was air-sealed using mastic sealant; the integrity of the seal was verified by seeding glycerin particles into a flow of air through the duct, and visually confirming no air leakage. This leak test was performed with the GSAC supply-air ESP (DP 3319) greater than 250 Pa; in comparison, the typical ESP during the GSAC tests was ≈60 Pa.

3.3 Liquid-side measurements and components

The GSHX HTF was an antifreeze solution of water/ethanol/isopropanol 70/25/5 % by mass (freeze protection to -9.5 °C) [47]. The liquid-side heat transfer in the condenser/gas-cooler was characterized by measurements (Fig. 5, Fig. 11) of mass flow using a coriolis meter (MF 3402), temperature difference using RTDs 1600 and 1601 inserted in the stream with thermowells (Table 7), and published data for the HTF heat capacity (Table 9) [47]. The coriolis meter also measured the HTF density (D 3502). A rotameter was used to verify the flowrate and to provide visual confirmation that no air bubbles were entrained in the liquid. The ELT was measured by RTD 3604. The HTF temperature exiting the GSAC was measured using RTD 3602, which was redundant with RTD 1601. GSAC inlet and differential pressures were measured, respectively, with transducers P 3317 and DP 3318; redundant analog gauges verified these transducer measurements. There were additional pressure transducers on the GSAC at the inlet and exit of the condenser/gas-cooler (P 1217 and 1218). The power and total energy input to the pump integrated with the CO_2 GSAC were measured, respectively, using W 1305 and Wh 1405.

The electrical power input to the circulation heater (W 3300) was measured for control and diagnostic purposes (e.g. heater power above 10 kW would indicate abnormal operation), as well as for calculating the HTF specific heat.

The primary components (Table 7) used to regulate the HTF flow and temperature were a water-cooled chiller (with vented reservoir) and an electric circulation heater. The chiller provided coarse control (resolution ± 0.5 °C), and the heater provided fine control (resolution ± 0.01 °C) and trimmed the HTF ELT to the desired value. The heater was able to maintain ELT stability to within ±0.04 °C maximum deviation from the setpoint. The circulation heater was powered by a silicon-controlled rectifier (SCR) controlled by a proportional-integral-derivative (PID) controller (whose process signal came from 'RTD PID', which nearly equaled the readings from RTD 3604 (Fig. 11)). The apparatus had two manually-operated valves in parallel to control the flow rate: a gate valve for course adjustment and needle valve for fine adjustment. Only the needle valve was required for these tests.

A safety circuit (Fig. 11) disengaged the SCR contactor if any of the safety switches detected conditions outside the safety limits. The safety switches (Table 7) were located after the circulation heater and included: a low-pressure switch (PS-L), a high-pressure switch (PS-H), a flow switch (FS), an in-stream temperature switch (TS 65), and a temperature limit controller (TLC) switch with a thermocouple directly attached to the heater-element surface. The low-pressure switch ensured the pressure was above 100 kPag to increase the boiling point of ethanol in the HTF (97 °C at 100 kPag vs. 78 °C at 0 kPag,). Note that ethanol was the constituent with the lowest boiling point, and therefore caused the most concern regarding boiling dryout in the circulation heater. A pressure relief valve opened if the HTF pressure rose above 700 kPag.

Miscellaneous components (Table 7) included the expansion tank to regulate pressure, especially for future tests for GSHPs in heating mode (not discussed here) when the chiller and its associated vented reservoir would be valved off. A filter was used to control contaminants. EPDM-rubber garden hoses were used for filling and draining the HTF since the ethanol is not chemically compatible with typical plastics used in garden hoses. All components were connected using 25 mm ID copper tubing, and the components and tubing were insulated with 13 mm of closed-cell foam (R-value 0.36 $m^2 \cdot K/W$).

3.4 Operation

3.4.1 Test targets and tolerances

There were a total of ten tests with the GSAC: the four ISO 13256-1 tests (Table 10) 'standard', 'part load', 'minimum', 'maximum'; the five 'extended ELT' tests (Table 11) 'ELT-1,2,3,4,5'; and one repeat of the 'standard' test condition. The 'extended ELT' tests were carried out to refine the characterization of the GSAC performance over the range of ELTs expected during typical operation. The ELT for the 'maximum' condition was 39 °C, because with the

40 °C specified by ISO 13256-1 the high-side pressures exceeded the 10 000 kPa measurement limit of the pressure transducers.

The test conditions based on ISO 13256-1 included return-air dry-bulb and dew-point temperatures, as well as the ELT. Further, the ISO standard requires the airflow and liquid flow rates to match values specified by the manufacturer; since the unit is an in-house prototype, the values were selected based on nominal values for GSHPs. The targeted airflow and liquid flow rates were 342 L/s and 0.2839 L/s (Table 10), respectively. When normalized by the nominal 'standard' condition capacity of 6660 W, the airflow and liquid flow were 5.14×10^{-2} L/(s·W) and 4.26×10^{-5} L/(s·W), respectively (383 CFM/ton and 2.38 GPM/ton). The imposed test conditions complied with the tolerances specified by ISO 13256-1 [39] (Table 12). Per ISO 13256-1 ([39], Section 4.2.4) the GSAC was operated for at least 1 h before beginning to record measurements included in the steady-state window; typically the unit required (2 to 4) h of operation at the test condition to reach steady state.

3.4.2 Test apparatus control

The GSAC compressor speed was fixed at 50 Hz using the inverter. Fixed speeds were also used for the GSAC fan and pump; the fan was set using the AHU control board (AC/HP Size: 8.8 kW, CFM adjust: Lo, and Dehumidify: Normal), and the pump flow was adjusted using the built-in speed-adjustment screw (set to 80 %). Nominal operating values were: capacity 6600 W, airflow 342 L/s, and liquid flow 17 L/min. The EEV controller was programmed to regulate the evaporator-outlet superheat between (5 and 7) °C. The refrigerant charge was adjusted to achieve the condenser-exit subcooling target (5 ± 0.5) °C at the 'standard' test condition. The refrigerant charge for all tests presented here was (3040 ± 10) g.

Air-side control consisted of using the booster fan to control the GSAC supply-air ESP to the targeted value, 58 Pa (Table 10, Table 11). The ISO 13256-1 standard requires using the supply-ESP target provided by the manufacturer, but this is an in-house prototype, so no such value exists. We selected the target value to be greater than 25 Pa; this was guided by the requirement of the AHRI 210/240 standard ([48], section 6.1.3.6), though the standard doesn't technically apply here since it is only intended for ASHPs. The value was also chosen to be less than the nominal maximum for typical residential heat pump applications, about 200 Pa based on our experience.

For the liquid-side control, the flow rate was manually adjusted using the needle valve. The HTF temperature entering the GSAC (ELT) was regulated in partnership by the chiller and the circulation heater. The chiller was set to 1 °C below the ELT target, and the circulation-heater PID controller was set at the ELT target.

Testing was initiated by setting the environmental chamber to the target dry-bulb and dew-point temperatures. Next, HTF flow through the GSAC was established using the chiller, and then the GSAC components were activated in the sequence of: (1) pump, (2) fan, and (3) compressor.

The booster fan was then turned on to control the GSAC supply-air ESP. After 30 minutes, the operator made final adjustments to the HTF flow rate, ELT, and GSAC supply-air ESP.

The laboratory operating procedure required the operator to lower the environmental chamber dry-bulb temperature below 27 °C before the GSAC was turned off, to prevent refrigerant pressures above the 7000 kPa burst-disc limit in the low-pressure-side cycle components. This procedural step was added after a system failure; the low-pressure burst disc ruptured and completely vented the refrigerant charge when the compressor was switched off with the return air at 32 °C and the AHU fan continued to move air through the evaporator, adding heat to the refrigerant. The CO_2 pressure had quickly risen above the 7000 kPa burst-disc limit, since the associated CO_2 saturation temperature is only 28.7 °C.

4 Data Analysis

4.1 Refrigerant-side calculations

The thermodynamic states numbered 1 through 13 (Fig. 5) were calculated using two intensive properties defined by the measurements and equations in Table 13. Thermodynamic properties for CO_2 were computed using a software package [49], which uses the equation of state developed by [50]. The NIST 'Reference Fluid Thermodynamic and Transport Properties Database' (REFPROP) [10] were used to verify the property data in [49].

4.1.1 *Energy transfers*

The evaporator and condenser/gas-cooler energy transfers were calculated as:

$$Q_{\text{cond,ref}} = m_{\text{ref}}\left(i_2 - i_5\right) \tag{4.1}$$

$$Q_{\text{evap,ref}} = m_{\text{ref}}\left(i_{10} - i_8\right) \tag{4.2}$$

where m_{ref} was the refrigerant mass flow rate, kg/s; i_2 was the condenser/gas-cooler inlet enthalpy, kJ/kg; i_5 was the condenser/gas-cooler outlet enthalpy, kJ/kg; i_8 was the evaporator inlet enthalpy, kJ/kg; and i_{10} was the evaporator outlet enthalpy, kJ/kg. These refrigerant energy transfer measurements were compared with those for the HTF (in the condenser/gas-cooler) and air (in the evaporator) defined in Sections 4.2 and 4.3 and discussed in Section 5.10.

4.1.2 *Compressor efficiency*

The total compressor efficiency was defined as the ratio of work required for isentropic compression to the electrical input to the motor ([51], Ch. 38: Compressors):

$$\eta_{\text{total}} = \frac{m_{\text{ref}}\left(i\left(P_1, s_{13}\right) - i_{13}\right)}{W_{\text{com}}} \tag{4.3}$$

where P_1 was the discharge pressure, kPa; $i(P_1, s_{13})$ was the discharge enthalpy if the compression had been isentropic, kJ/kg; s_{13} was the compressor suction entropy, kJ/(kg·K); i_{13} was the suction enthalpy, kJ/kg; and W_{com} was the compressor electric power, W. The heat loss ratio quantified the fraction of compressor electric power dissipated as heat from the compressor to the ambient air:

$$\gamma_{\text{com}} = 1 - \frac{m_{\text{ref}}\left(i_1 - i_{13}\right)}{W_{\text{com}}} \tag{4.4}$$

where i_1 was the discharge enthalpy, kJ/kg. Finally, the compressor volumetric efficiency was calculated as:

$$\eta_{\text{v}} = \frac{m_{\text{ref}}\ v_{13}}{V_{\text{d}}} \tag{4.5}$$

where v_{13} was the suction specific volume, m^3/kg; and the compressor displacement was:

$$V_\mathrm{d} = \mathrm{N_{cyl}} \frac{\pi\, D_\mathrm{b}^2\, L_\mathrm{s}/4}{\mathrm{rev}} \frac{1450\ \mathrm{rev/min}}{60\ \mathrm{s/min}} \frac{f}{50\ \mathrm{Hz}} \tag{4.6}$$

where D_b was the cylinder bore diameter, mm; L_s was the cylinder stroke, mm; $\mathrm{N_{cyl}}$ was the number of cylinders, 2; and f was the excitation frequency provided by the inverter to the compressor, which was fixed at 50 Hz for the data presented here (Table 2, note that the V_d units in the table are m^3/h, whereas the units in Eq. (4.6) are mm^3/s). The fraction representing the compressor speed, 1450 RPM, at an inverter frequency of 50 Hz, was specified in the manufacturer's datasheet [52].

4.1.3 LLSL-HX effectiveness

The LLSL-HX effectiveness was computed as the ratio of the heat transferred on the vapor side ($Q_\mathrm{LLSL,vap}$), W, to the maximum possible heat transfer ($Q_\mathrm{LLSL,max}$), W. The vapor specific heat ($c_\mathrm{p,LLSL,vap}$), kJ/(kg·K), was always less than the liquid specific heat ($c_\mathrm{p,LLSL,liq}$), kJ/(kg·K), so the equation reduced to a ratio of temperatures:

$$\varepsilon_\mathrm{LLSL} = \frac{Q_\mathrm{LLSL,vap}}{Q_\mathrm{LLSL,max}} = \frac{c_\mathrm{p,LLSL,vap}\left(T_{12} - T_{11}\right)}{\mathrm{MIN}\left(c_\mathrm{p,LLSL,vap}, c_\mathrm{p,LLSL,liq}\right)\left(T_5 - T_{11}\right)} = \frac{T_{12} - T_{11}}{T_5 - T_{11}} \tag{4.7}$$

4.1.4 LLSL-HX impact on cycle efficiency

The impact of the LLSL-HX on the cycle efficiency was calculated by comparing the measured COP for the cycle with the LLSL-HX to the estimated COP without the LLSL-HX, for the same capacity, evaporator-outlet superheat, airflow, HTF flow, and ELT. Neglecting the fan and pump power, the COP of the cycle with the LLSL-HX for the tests presented here was:

$$\mathrm{COP_{LLSL}} = \frac{Q_\mathrm{evap,ref}}{W_\mathrm{com}} = \frac{m_\mathrm{ref}\left(i_{10} - i_8\right)}{m_\mathrm{ref}\left(i\left(P_1, s_{13}\right) - i_{13}\right)/\eta_\mathrm{total}} \tag{4.8}$$

Note that $\mathrm{COP_{LLSL}}$ is only used in the evaluation of the impact of the LLSL-HX on the cycle. The ISO 13256-1 rated efficiency of the CO_2 GSAC, $\mathrm{COP_{adj}}$, is defined in Section 4.4.

The evaporator capacity without the LLSL-HX (i.e. a basic cycle) was assumed to equal the measured capacity with the LLSL-HX. This would be achieved, for example, by adjusting the compressor speed using the inverter. The COP of the cycle without the LLSL-HX was estimated as:

$$\mathrm{COP_{basic}} = \frac{Q_\mathrm{evap,ref,basic}}{W_\mathrm{com,basic}} = \frac{m_\mathrm{ref,basic}\left(i_{10} - i_5\right)}{m_\mathrm{ref,basic}\left(i\left(P_1, s_{10}\right) - i_{10}\right)/\eta_\mathrm{total}} \tag{4.9}$$

where $Q_{evap,ref,basic}$ was the evaporator capacity, W; $W_{com,basic}$ was the compressor work, W; $m_{ref,basic}$ was the refrigerant mass flow rate; and s_{10} was the evaporator-outlet entropy, kJ/(kg·K). This simplified analysis included a number of assumptions:

1) The differences in refrigerant-side evaporator pressure drop and heat-transfer coefficients, due to differences in mass flow with or without the LLSL-HX, were neglected. The same assumption was applied for the condenser/gas-cooler.
2) Differences in evaporator saturation temperature with or without the LLSL-HX were neglected since the differences in the evaporator pressure drop were ignored (i.e. assumption 1) and the capacities were the same. Also, the evaporator-outlet superheat was held constant. Therefore, the evaporator-outlet enthalpy without the LLSL-HX was assumed to equal the measured value with the LLSL-HX, i_{10}.
3) The evaporator-inlet enthalpy without the LLSL-HX was assumed to equal the condenser-outlet enthalpy from the measurements with the LLSL-HX, i_5. This includes an assumption of isenthalpic expansion across the EEV. Further, this neglects any differences in condenser saturation pressure associated with differing heat rejection (caused by changes in efficiency) or pressure drop.
4) The compressor efficiency, η_{total}, was assumed to be the same with or without the LLSL-HX.

The estimated refrigerant mass flow rate without the LLSL-HX was calculated using the numerators of Eqs. (4.8) and (4.9), and the assumption of equal capacity with and without the heat exchanger:

$$m_{\text{ref,basic}} = m_{\text{ref}} \left(\frac{i_{10} - i_8}{i_{10} - i_5} \right) \tag{4.10}$$

Combining Eqs. (4.8), (4.9), and (4.10), the ratio of COP with and without the LLSL-HX was:

$$\frac{\text{COP}_{\text{LLSL}}}{\text{COP}_{\text{basic}}} = \left(\frac{i_{10} - i_8}{i_{10} - i_5} \right) \left(\frac{i(s_{10}, P_1) - i_{10}}{i(s_{13}, P_1) - i_{13}} \right) \tag{4.11}$$

where the first bracketed fraction quantifies the effect of the LLSL-HX on the mass flow rate and the second fraction captures the change in compressor work per mass flow. This analysis is similar to the one presented in [53].

4.2 Air-side calculations

The moist airflow rate, in $\text{m}^3_{\text{ma}}/\text{s}$, through a single nozzle [39], [45] was calculated by:

$$V_{\text{n}} = C_{\text{d}} A_{\text{n}} \sqrt{2\, \Delta P_{\text{n}}\, v'_{\text{n}}} \tag{4.12}$$

$$v'_{\text{n}} = \frac{v_{\text{n}}}{1 + \omega_{\text{n}}} \tag{4.13}$$

where C_d was the nozzle discharge coefficient; A_n was the flow area of the nozzle throat, m^2; ΔP_n was the static pressure difference across the nozzle, Pa (DP 3320); v'_n was the moist-air specific volume of air at the nozzle, m^3_{ma} / kg_{ma} ; v_n was the dry-air specific volume of air at the nozzle, m^3_{ma} / kg_{da} ; and ω_n was the air humidity ratio computed using the dewpoint measurement (Dew 3506) and ([54], Chapter 1 'Psychometrics'), kg_w / kg_{da}. For future tests with multiple nozzles (only nozzle #4 was used here, Table 8), the total airflow rate would be the sum of the flow rates of the individual nozzles.

The nozzles have a throat-to-diameter ratio of 0.6 per [46], so the nozzle discharge coefficient was calculated as [45], [46]:

$$C_d = 0.9986 - \frac{7.006}{\sqrt{Re}} + \frac{134.6}{Re} \tag{4.14}$$

$$Re = \frac{D_n}{\mu_n \, v'_n} C_d \sqrt{2 \, \Delta P_n \, v'_n} \tag{4.15}$$

where Re was the nozzle Reynold's number; D_n was the nozzle throat diameter, m; μ_n was the dynamic air viscosity at the nozzle inlet, kg/(m·s) ([54], Chapter 1: Psychometrics).

4.3 Liquid-side calculations

The energy transferred in the condenser/gas-cooler to the HTF was:

$$Q_{cond,liq} = m_{liq} \, c_{p,liq,cond} \left(T_{liq,cond,out} - T_{liq,cond,in} \right) \tag{4.16}$$

where m_{liq} was the HTF mass flow rate (MF 3402 in Fig. 5), kg/s; $c_{p,liq,cond}$ was the specific heat of the HTF (Table 9) [47] evaluated at the average temperature in the condenser/gas-cooler, kJ/(kg·K); and $T_{liq,cond,out}$ and $T_{liq,cond,in}$ (i.e. ELT) were the condenser/gas-cooler HTF outlet and inlet temperatures, °C (RTDs 1600 and 1601 in Fig. 5).

4.4 Overall GSAC system performance

The ISO 13256-1 standard [39] prescribes corrections to the capacity and power input for GSHPs with integral fans and pumps, so that 'only the portion of the fan/pump power required to overcome the internal resistance' of the GSAC is included. Therefore, a correction was applied for the extra fan power needed to move the air through the ductwork after the GSAC, including the nozzle section. The correction was subtracted from the electrical energy input and added to the cooling capacity (since the extra power input was dissipated as heat into the airstream and effectively reduced the system capacity). The measured fan power, W_{fan} (W 1306 in Fig. 5), was corrected by:

$$W_{fan,correction} = \frac{V_{fan} \, \Delta P_{ext,air}}{\eta_{fan}} \tag{4.17}$$

where V_{fan} was the fan flow rate, m^3_{ma}/s; $\Delta P_{ext,air}$ was the external static pressure difference (DP 3319 in Fig. 5, Fig. 7), Pa; and η_{fan} was the nominal fan efficiency, 0.3, given by ISO 13256-1 [39]. The fan airflow rate was calculated as:

$$V_{fan} = V_n \frac{v_{fan}}{v_n} \tag{4.18}$$

where v_{fan} was the dry-air specific volume of the supply air, m^3_{ma}/kg_{da}.

The adjusted sensible cooling capacity was calculated by adding the fan correction to the sensible capacity measured by the air-side instruments:

$$Q_{sens,adj} = \frac{V_n}{v_n} c_{p,air} \left(T_{air,return} - T_{air,supply}\right) + W_{fan,correction} \tag{4.19}$$

where $T_{air,return}$ was the average of associated RTDs (3700, 3701, and 3702), °C; $T_{air,supply}$ was the average of associated RTDs (3703, 3704, and 3705), °C; and the air specific heat, $c_{p,air}$, kJ/(kg$_{da}$·K) was calculated as [39]:

$$c_{p,air} = 1006 + 1860\, \omega_{air,supply} \tag{4.20}$$

The latent capacity was unaffected by the fan adjustment:

$$Q_{lat} = i_{fg,w} \frac{V_n}{v_n} \left(\omega_{air,return} - \omega_{air,supply}\right) \tag{4.21}$$

where $\omega_{air,return}$ and $\omega_{air,supply}$ were respectively the humidity ratios of the return and supply air calculated using the Dew 3504 and Dew 3506 measurements, respectively, kg_w / kg_{da}; and $i_{fg,w}$ was the latent heat of vaporization of water at 15 °C, 2470 kJ/kg [39]. The total adjusted capacity was the sum of the sensible and latent values:

$$Q_{total,adj} = Q_{sens,adj} + Q_{lat} \tag{4.22}$$

The adjusted sensible heat ratio was therefore:

$$\mathrm{SHR}_{adj} = \frac{Q_{sens,adj}}{Q_{total,adj}} \tag{4.23}$$

A similar correction was applied to the GSAC pump power, W_{pump} (W 1305 in Fig. 5), per the ISO 13256-1 standard. The portion of the GSAC-pump electric power used to push the heat transfer fluid through the test apparatus and instruments (Fig. 5) was subtracted from the total power input:

$$W_{pump,correction} = \frac{V_{pump}\, \Delta P_{liq}}{\eta_{pump}} \tag{4.24}$$

where V_{pump} was the pump flow rate of liquid, computed using the mass flow rate (MF 3402 in Fig. 5) and density (D 3502) measurements, m^3/s, ΔP_{liq} was the liquid static pressure difference

(DP 3318), kPa; and the nominal pump efficiency, η_{pump}, was the same value used for the fan, 0.3, per the ISO standard [39]. The total adjusted power input to the GSAC was therefore:

$$W_{\mathrm{total,adj}} = W_{\mathrm{com}} + \left(W_{\mathrm{pump}} - W_{\mathrm{pump,correction}}\right) + \left(W_{\mathrm{fan}} - W_{\mathrm{fan,correction}}\right) \tag{4.25}$$

Finally, the adjusted coefficient of performance was defined as:

$$\mathrm{COP}_{\mathrm{adj}} = \frac{Q_{\mathrm{total,adj}}}{W_{\mathrm{total,adj}}} \tag{4.26}$$

Note that this COP (rather than the one defined in Eq. (4.8)) represents the ISO 13256-1 rated efficiency and is the COP discussed in Section 5.1.

4.5 Energy transfer measurement imbalances

Imbalances in the energy transfer measurements serve as a quality metric for the test data. The imbalance of the condenser energy transfers was:

$$\Delta Q_{\mathrm{imb,cond}} = \frac{Q_{\mathrm{cond,ref}} - Q_{\mathrm{cond,liq}}}{\left(Q_{\mathrm{cond,ref}} + Q_{\mathrm{cond,liq}}\right)/2} \tag{4.27}$$

where the denominator was the average of the heat transfer on the refrigerant and liquid sides. The evaporator energy transfer measured on the air side was defined as:

$$Q_{\mathrm{evap,air}} = \frac{V_{\mathrm{n}}}{v_{\mathrm{n}}} c_{\mathrm{p,air}} \left(T_{\mathrm{air,return}} - T_{\mathrm{air,supply}}\right) + Q_{\mathrm{lat}} + W_{\mathrm{fan}} \tag{4.28}$$

where the heat input from the fan, W_{fan}, was added to the air-side sensible and latent capacities. This addition was required to account for all the air-side evaporator energy transfer, since the fan heated the air after it went through the evaporator, and the air-side temperature sensors (RTD 3703, 3704, and 3705) used to compute the sensible capacity were located after the fan. Next, the imbalance of the evaporator energy transfers was computed as:

$$\Delta Q_{\mathrm{imb,evap}} = \frac{Q_{\mathrm{evap,ref}} - Q_{\mathrm{evap,air}}}{\left(Q_{\mathrm{evap,ref}} + Q_{\mathrm{evap,air}}\right)/2} \tag{4.29}$$

Lastly, a system energy imbalance was defined for the GSAC:

$$\Delta Q_{\mathrm{imb,sys}} = \frac{W_{\mathrm{com}} + W_{\mathrm{fan}} + \frac{V_{\mathrm{n}}}{v_{\mathrm{n}}} c_{\mathrm{p,air}} \left(T_{\mathrm{air,return}} - T_{\mathrm{air,supply}}\right) + Q_{\mathrm{lat}} - Q_{\mathrm{cond,liq}}}{\left(W_{\mathrm{com}} + W_{\mathrm{fan}} + \frac{V_{\mathrm{n}}}{v_{\mathrm{n}}} c_{\mathrm{p,air}} \left(T_{\mathrm{air,return}} - T_{\mathrm{air,supply}}\right) + Q_{\mathrm{lat}} + Q_{\mathrm{cond,liq}}\right)/2} \tag{4.30}$$

which represents an accounting of the energy crossing the boundary of the GSAC including the electricity, airflow, and HTF flow. Note that the pump electrical energy, W_{pump}, is not in Eq. (4.30) because the condenser-inlet liquid temperature measurement (RTD 1600) used to calculate $Q_{cond,liq}$ was located after the pump (Fig. 5). Eq. (4.30) also neglects the energy transfers from the GSAC components to the ambient air surrounding the unit.

5 Experimental results

This section shows the results of the measurements and calculations described in Sections 3 and 4. The measurement uncertainties were computed by propagating the instrument uncertainty (Table 6) through the equations presented in Section 4. The uncertainty propagation calculations were performed using a software package [49]. All uncertainties in the proceeding figures and tables are reported as expanded uncertainties, with $k = 2$ (95 % confidence interval, CI). The nominal GSAC measurement uncertainties were: ±4 % for COP, ±275 W (≈4 %) for total capacity, and ±150 W (≈3 %) for sensible capacity.

Note that the performance figures (Fig. 12 through Fig. 23) are annotated with the test conditions (e.g. 'standard', 'ELT-1') defined in Table 10 and Table 11. Also, note all the figures are presented with ELT (RTD 3604) as the dependent variable. While the performance metrics generally correlate well to ELT, ELT may not be the best or only correlation variable. Nevertheless, for consistency, ELT is used in all these figures. All measurements and calculated performance metrics are shown in Appendix A (Table A-1, Table A-2); those values were used to create the figures discussed in this section.

5.1 COP, capacity, and SHR for the CO2 system

The COP and capacity decreased significantly with increasing ELT, while the SHR increased (Fig. 12). At 'standard' conditions the COP was 4.14, the total capacity was 6660 W, the sensible capacity was 5340 W, and the SHR was 0.80. For the 'part-load' conditions the COP was 4.92, the total capacity was 7240 W, the sensible capacity was 5640 W, and the SHR was 0.78. The COP was lower for 'minimum' than 'ELT-1', because the return-air temperature was lower for the 'minimum' test condition (21 °C) than the 'ELT-1' test condition (27 °C). The lower temperature increased the lift and reduced COP, per the Carnot efficiency.

The tests for this report were performed using the water/ethanol/isopropanol antifreeze HTF Table 9 [47]. An additional set of repeated tests was performed using water as the HTF. The results are not presented here, but the COP and capacity were nominally equivalent as the differences were within the uncertainty bars for all test conditions.

5.2 Comparison with commercially-available R410A GSHP

The COP, capacity, and SHR of the CO_2 GSAC were compared to manufacturer's data [40] for a R410A GSHP (Fig. 12) that was similarly-sized, commercially-available, and at an entry-level price point (i.e. relatively low cost). The R410A GSHP manufacturer followed the same ISO 13256-1 standard for the data collection and reduction, including adjustments to the fan and pump power. At the 'standard' condition, the R410A GSHP cooling capacity was 6770 W (≈2 ton), the COP was 4.57 (EER of 15.6 Btu/(h·W)), and the SHR was 0.72. In comparison the CO_2 GSAC COP was 4.14 and the SHR was 0.80. At the 'part-load' condition the CO_2 and R410A system COPs were about 4.92, and the total capacities were very similar. The 'part-load' COP and capacity for the R410A GSHP were within the uncertainty bars for the CO_2 GSAC measurements. The R410A GSHP 'part-load' SHR was 0.71, compared to 0.78 for the CO_2 GSAC.

At lower ELTs ('ELT-1,2') the CO_2 GSAC had higher COP and total capacity than the R410A system; at higher ELTs ('ELT-3,4,5') the R410A had higher values. The CO_2 GSAC had a higher sensible capacity and correspondingly a higher SHR across the entire ELT range. The R410A unit was therefore better at removing moisture from the air.

5.3 Operating pressures

The CO_2 operating pressures (Fig. 13) were of particular interest, since they were much higher than for a conventional R410A system (e.g. R410A condenser saturation pressure is ≈2400 kPa at a saturation temperature of 40 °C). The pressures were not explicitly controlled, but rather determined by GSAC system equilibrium established by the temperatures of the HTF and the air, the heat transfer resistance in the evaporator and condenser/gas-cooler, the compressor pressure/flow relationship, the EEV-regulated superheat, and the refrigerant charge.

For the 'ELT-5' and 'maximum' tests, with ELT respectively at 36.8 °C and 39 °C, the condenser/gas-cooler average pressures were about 9500 kPa, though some individual readings comprising the average approached 10 000 kPa. The largest pressure on the low-pressure side was about 5500 kPa, for the 'maximum' test.

5.4 Condenser/gas-cooler heat transfer

In subcritical mode the GSAC CO_2 cycle operated near the top of the fluid two-phase dome (Fig. 14 (a)), so a large, and sometimes dominant fraction of condenser/gas-cooler heat transfer occurred in the vapor region. The fraction of heat transfer in the single-phase regime increased with ELT (Fig. 15). For transcritical operation (Fig. 14 (a)) the condenser/gas-cooler heat transfer occurred with the CO_2 entirely in a supercritical state.

The condenser/gas cooler heat transfer profile for the CO_2 GSAC was markedly different than that of conventional GSHPs using R410A. For R410A systems, most of the condenser heat transfer is with the refrigerant in the two-phase regime (Fig. 14 (b)). Note that the R410A cycle thermodynamic states shown in Fig. 14 (b) were computed using a simple simulation for a heat pump without a LLSL-HX, at the 'standard' test condition, with no pressure drop in the heat exchangers, and log-mean temperature differences of 2 °C in the condenser and 10 °C in the evaporator.

5.5 Compressor efficiency

The CO_2 GSAC total compressor efficiency ranged (0.40 to 0.56) and increased with the ELT, while the volumetric efficiency ranged (0.76 to 0.89) and decreased with increased ELT (Fig. 16). These trends agree with data from the compressor manufacturer's datasheet [52] (Fig. 17). The compressor pressure ratio (P_1/P_{13}, discharge/suction pressures, kPa/kPa) had a relatively narrow range for these tests, about 1.2 to 2.1, and the pressure ratio increased with ELT. For the total compressor efficiency, we observed only a minor quadratic correlation to pressure ratio, as opposed to the strong quadratic and cubic inflections shown in the manufacturer's data at pressure ratios ranging (1 to 5). For volumetric efficiency, both our test results and the manufacturer's data had a linear correlation to pressure ratio.

The compressor heat-loss ratio increased with ELT (Fig. 18). This is physically consistent with the higher discharge temperatures measured with higher ELTs; the compressor shell is correspondingly warmer, which drives the additional heat loss.

5.6 Condenser/gas-cooler pinch-point temperature

The condenser/gas-cooler pinch-point temperature (the minimum temperature difference between the refrigerant and liquid, which here always occurred at the cold end) was very small; the uncertainty band always included 0 °C (Fig. 19). A small condenser/gas-cooler pinch-point temperature difference is particularly important for CO_2 systems (compared to HFC systems) to minimize the throttling losses [12], though in this case the heat exchanger may have been larger than necessary.

5.7 LLSL-HX effectiveness

The LLSL-HX effectiveness ranged (0.83 to 0.96) and increased with ELT (Fig. 20). At low ELTs the effectiveness uncertainty was large because little heat was transferred, and therefore the fluid temperature change was small relative to the ±0.6 °C thermocouple uncertainty (Table 6). When the ELT was 15 °C or less, the refrigerant liquid temperature exiting the condenser/gas-cooler approached the evaporator outlet temperature, so there was little temperature difference to drive heat transfer.

5.8 LLSL-HX impact on cycle efficiency

The LLSL-HX increased the refrigerant subcooling and therefore reduced the enthalpy of the refrigerant entering the evaporator (from state 5 to 6, Fig. 14 (a)). This increased the enthalpy difference of the refrigerant in the evaporator (state 8 to 10, Fig. 14 (a)), reducing the mass flow required to achieve the target capacity (compared to a basic cycle without a LLSL-HX). The increase in evaporator enthalpy difference equals the enthalpy change of the refrigerant in the LLSL-HX [53]. However, the LLSL-HX also increased the superheat and subsequently the mass-flow-specific compressor work. The balance of these opposing effects determined how the inclusion of the LLSL-HX affected compressor power and therefore COP (the analysis constrained the evaporator capacity to be the same with and without the LLSL-HX, so the COP difference is only manifested through the change in compressor power).

Using the performance prediction of the cycle without the LLSL-HX (Section 4.1.4), the LLSL-HX was estimated to have caused a COP penalty of (0 to 2) % for ELTs ranging (10 to 25) °C, and a benefit of (0 to 5) % for ELTs ranging (30 to 39) °C. The benefit of the LLSL-HX at higher ELTs, where the system operated with a transcritical cycle, agrees with the results reported by ([24], [25]) for transcritical CO_2 ASHPs; however the benefit was somewhat small since the GSAC operated closer to the border of subcritical and transcritical cycles. For lower

ELTs where the CO_2 GSAC operated in a subcritical cycle, the LLSL-HX did not provide a benefit or even caused a penalty to the COP.

5.9 Superheat and subcooling

The evaporator-outlet superheat was controlled by the EEV and superheat controller, and therefore had a narrow range of (4.7 to 5.5) °C (Fig. 22). The condenser-exit subcooling was not controlled so it had a larger range of (5.3 to 7.5) °C. The subcooling decreased with increasing ELT (Fig. 22). With the ELT greater than 25 °C the system operated in a transcritical cycle so the subcooling was undefined (shown as '0' subcooling in Fig. 22).

The accumulator had an important role in protecting the compressor by preventing liquid carryover into the compressor suction port (which can cause cavitation and damage the compressor). This was especially important for the tests with lower ELTs where the LLSL-HX only minimally increased, or even *decreased*, the superheat. At the 'minimum' test condition with ELT 10 °C the LLSL-HX only increased superheat from 5.0 °C to 6.2 °C. For the 'ELT-1' test condition with ELT 10 °C the LLSL-HX decreased the superheat from 5.1 °C to 3.5 °C.

5.10 Energy transfer measurement imbalances

The imbalances in the energy transfer measurements in the evaporator and condenser/gas-cooler were tracked as a data-quality measure (Fig. 23 (a)). The transferred energy measured on the refrigerant and HTF sides in the condenser/gas-cooler matched within (-2.5 to -1.0) %, where the negative sign indicates the liquid-side energy transfer measurement was larger, Eq. (4.27). The evaporator imbalance ranged (1.7 to 3.8) %, where the positive sign means the refrigerant-side energy transfer measurement was larger, Eq. (4.29). The error bars for the evaporator imbalance were relatively large because of the air-side measurements of dew-point temperature and airflow, which have relatively large uncertainties (Table 6, Section 3.2). The ISO 13256-1 [39] standard does not require a particular energy imbalance, though a related standard, ANSI/ASHRAE 206-2017 ([55], section 9.1.3), requires the primary capacity measurement (air-side) to match the secondary measurement (e.g. refrigerant-side or liquid-side capacity) within ±5 %. By that measure, all the present tests were acceptable. Further, the imbalances in the GSAC system-level energy measurements, Eq. (4.30), were all less than ±5 % (Fig. 23 (b)).

6 Conclusions and Future Work

A prototype CO_2 GSAC was tested in a laboratory. The GSAC implements the basic vapor-compression cycle modified to incorporate a LLSL-HX. Cycle components included: a semi-hermetic compressor, brazed-plate heat exchangers for the condenser/gas-cooler and the LLSL-HX, a fin-tube evaporator coil, and an EEV with a superheat controller. The GSAC was tested according to the ISO standard for liquid-to-air heat pumps (ISO 13256-1), with test conditions including: 'standard', 'part-load', 'minimum', and 'maximum'. The system performance was very sensitive to ELT, so the GSAC was tested at five additional ELTs ('ELT-1,2,3,4,5') ranging (10 to 36.8) °C to provide more granular data.

The LLSL-HX was estimated to have caused a COP penalty of about (1 to 2) % for ELTs ranging (10 to 25) °C, and a benefit of (0 to 5) % for ELTs ranging (30 to 39) °C. The estimation compared the measurements of the CO_2 GSAC with the LLSL-HX to predicted cycle performance without the LLSL-HX. The benefit of the LLSL-HX at higher ELTs, where the system operated with a transcritical cycle, agrees with the results reported by ([24], [25]) for transcritical CO_2 ASHPs; however the benefit was somewhat small since the GSAC operated closer to the border of subcritical and transcritical cycles. For lower ELTs where the CO_2 GSAC operated in a subcritical cycle, the LLSL-HX did not provide a benefit or even caused a penalty to the COP. The net benefit/penalty of the LLSL-HX would depend on the fraction of time the system operated in a subcritical or transcritical cycle. Considering the relatively small benefit for the transcritical cycle, and that the goal of the ground-source (as opposed to air-source) system is to operate more often in a subcritical cycle, the LLSL-HX is probably not a good option. The system throttling irreversibilities may be better mitigated using an economizer or a work-recovery expansion device, such as an expander or ejector.

The CO_2 GSAC results were compared to manufacturer's data for a relatively low-cost, commercially-available R410A GSHP. The ISO 13256-1 'standard' test condition (ELT 25 °C) cooling COP for the CO_2 GSAC was 4.14, compared to the R410A GSHP with a COP of 4.57. At the 'part-load' conditions (ELT 20 °C) the CO_2 system had a COP of 4.92, which nominally equaled the R410A GSHP value. At lower ELTs ('ELT-1,2'), (10 to 15) °C, the CO_2 GSAC had higher COP and total capacity than the R410A system; at higher ELTs ('ELT-3,4,5' and 'maximum'), (30 to 39) °C, the R410A system had higher values. The CO_2 system had a higher SHR across the entire ELT range, and therefore removed less moisture from the air. For the 'standard' and 'part-load' conditions the CO_2 GSAC SHRs were 0.80 and 0.78, respectively; for the R410A GSHP they were 0.72 and 0.71. To achieve similar dehumidification capability, the CO_2 system would need to operate with a lower evaporator saturation temperature, which could be accomplished, for example, by lowering airflow or increasing compressor speed. These changes would reduce the COP.

Recommendations for future work include improving the efficiency of the CO_2 GSAC. The efficiency is inversely proportional to the emissions from the power plant producing the electricity to drive the equipment, and those emissions essentially comprise the indirect emissions. Lee et al.

[11] showed that the indirect emissions comprised ≈90 % of the total lifetime emissions (sum of direct and indirect) for a R410A system. Since CO_2 has a GWP = 1 the direct emissions are essentially negligible for the CO_2 GSAC, so only the indirect emissions are significant. Consequently, to achieve a reduction in total lifetime emissions, the CO_2 system must be more than 90 % as efficient as an R410A system. The Hoseong et al. study [11] also showed that using an HFO/HFC blend could reduce the total lifetime emissions by ≈(4 to 7) % compared to a R410A system. To achieve similar total lifetime emissions, the CO_2 system would need to be (94 to 97) % as efficient as a R410A system. For the tests presented here, at the 'standard' condition the COP for the CO_2 GSAC was 4.14, which was 91 % of the commercially-available R410A system COP of 4.57. Assuming all operation was at the 'standard' condition, the CO_2 system would achieve nominally equivalent lifetime emissions as the R410A system but would have more total emissions than a system using an HFO/HFC blend. Therefore, to achieve lower emissions than current options, the CO_2 system efficiency must improve.

Suggestions for improving efficiency include reducing throttling losses by replacing the EEV with an ejector, or considering an economizer. Another recommendation for future work is modeling and experiments with the CO_2 system in heating mode. The heating mode could be favorable to CO_2 systems since their capacity stays relatively high at low temperatures, and they can avoid using inefficient auxiliary heat sources (e.g. electric-resistance heat, with COP = 1) [19]. This is important to consumers who will want the benefit of efficient heating provided by a GSHP (as opposed to the tested CO_2 GSAC, which only provides cooling) to offset the high initial cost of the GSHX. The prototype GSAC would need modification to operate in heating mode, including a reversing valve and a refrigerant-to-air heat exchanger with a higher pressure rating. The system efficiency would also benefit from operating as a combined appliance that provides hot water in addition to space conditioning, since the efficiency of CO_2-based HPWHs can exceed that of HFC-based systems [14]. A final recommendation is to study the annual performance of the CO_2 system while it is operating inside a residence. This could be accomplished, for example, using the annual building simulation of the NIST residential net-zero building [56]–[58]. The simulation would show the distribution of ELTs over the heating and cooling seasons, which would help to focus the efficiency-improvement effort in the most important temperature range.

7 References

[1] A. Pearson, "Carbon dioxide—new uses for an old refrigerant," *Int. J. Refrig.*, vol. 28, no. 8, pp. 1140–1148, 2005.

[2] T. J. Midgley, A. L. Henne, and R. McNary, "Heat transfer," U.S. Patent 1,833,847, 1931.

[3] IPCC, "Climate Change 2013: The Physical Science Basis. Contribution of Working Group I to the Fifth Assessment Report of the Intergovernmental Panel on Climate Change," [Stocker, T.F., D. Qin, G.-K. Plattner, M. Tignor, S.K. Allen, J. Boschung, A. Nauels, Y. Xia, V. Bex and P.M. Midgley (eds.)]. Cambridge University Press, Cambridge, United Kingdom and New York, NY, USA, http://www.climatechange2013.org/, 2013.

[4] EU, *Regulation (EU) No 517/2014 of the European Parliament and of the Council of 16 April 2014 on fluorinated greenhouse gases and repealing Regulation (EC) No 842/2006*. http://data.europa.eu/eli/reg/2014/517/oj, 2014.

[5] UNEP, *Amendment to the Montreal Protocol on Substances that Deplete the Ozone Layer, Kigali, 15 October 2016, C.N.872.2016.TREATIES-XXVII.2.f*. https://treaties.un.org/doc/Publication/CN/2016/CN.872.2016-Eng.pdf, 2016.

[6] ANSI/ASHRAE, "ASNI/ASHRAE Standard 34-2016: Designation and Safety Classification of Refrigerants." Amer. Soc. Heating, Ref. Air-Conditioning Eng. Inc., Atlanta, GA, 2016.

[7] P. A. Domanski, R. Brignoli, J. S. Brown, A. F. Kazakov, and M. O. McLinden, "Low-GWP refrigerants for medium and high-pressure applications," *Int. J. Refrig.*, vol. 84, pp. 198–209, 2017.

[8] M. O. McLinden, J. S. Brown, R. Brignoli, A. F. Kazakov, and P. A. Domanski, "Limited options for low-global-warming-potential refrigerants," *Nat. Commun.*, vol. 8, p. 14476, 2017.

[9] AHRI, "AHRI Low-GWP Alternative Refrigerants Evaluation Program." [Online]. Available: http://www.ahrinet.org/arep. [Accessed: 29-Aug-2019].

[10] E. W. Lemmon, I. H. Bell, M. L. Huber, and M. O. McLinden, "NIST Standard Reference Database 23: Reference Fluid Thermodynamic and Transport PropertiesP, Version 10.0." National Institute of Standards and Technology, USA, 2018.

[11] H. Lee, S. Troch, Y. Hwang, and R. Radermacher, "LCCP evaluation on various vapor compression cycle options and low GWP refrigerants," *Int. J. Refrig.*, vol. 70, pp. 128–137, 2016.

[12] M. H. Kim, J. Pettersen, and C. W. Bullard, "Fundamental process and system design issues in CO2 vapor compression systems," *Prog. Energy Combust. Sci.*, vol. 30, no. 2, pp. 119–174, 2004.

[13] G. Lorentzen, "Revival of carbon dioxide as a refrigerant," *Int. J. Refrig.*, vol. 17, no. 5, pp. 292–301, 1994.

[14] J. Stene, "Residential CO2 heat pump system for combined space heating and hot water

heating," *Int. J. Refrig.*, vol. 28, no. 8, pp. 1259–1265, 2005.

[15] Y. Hwang and R. Radermacher, "Theoretical evaluation of carbon dioxide refrigeration cycle," *HVAC&R Res.*, vol. 4, no. 3, pp. 245–263, 1998.

[16] G. Lorentzen and J. Pettersen, "A new, efficient and environmentally benign system for car air-conditioning," *Int. J. Refrig.*, vol. 16, no. 1, pp. 4–12, 1993.

[17] R. P. McEnaney, D. E. Boewe, J. M. Yin, Y. C. Park, and C. W. Bullard, "Experimental Comparison of Mobile A/C Systems When Operated with Transcritical CO2 Versus Conventional R134a, Paper #402," in *International Refrigeration and Air Conditioning Conference*, Purdue University, West Lafayette, IN, USA, 1998.

[18] J. S. Brown, S. F. Yana-Motta, and P. A. Domanski, "Comparitive analysis of an automotive air conditioning systems operating with CO2 and R134a," *Int. J. Refrig.*, vol. 25, no. 1, pp. 19–32, 2002.

[19] P. Neksa, "CO2 heat pump systems," *Int. J. Refrig.*, vol. 25, no. 4, pp. 421–427, 2002.

[20] J. Pettersen, R. Aarlien, P. Neska, G. Skaugen, and K. Aflekt, "A Comparitive Evaluation of CO2 and HCFC-22 Residential Air-conditioning Systems in a Japaneese Climate - Report HPC-WR-19," in *CO2 Technology in Refrigeration, Heat Pump, and Air Conditioning Systems - (Workshop Proceedings, May 13-14)*, Trondheim, Norway, 1997, pp. 177–191.

[21] Z. Jin, T. M. Eikevik, P. Neksa, A. Hafner, and R. Wang, "Energy efficiency comparison of heat pumping systems using R744 and R410A as refrigerant," in *Refrigeration Science and Technology - 12th IIR Gustav Lorentzen Natural Working Fluids Conference*, Edinburgh, Scottland, 2016, pp. 202–210.

[22] A. Jakobsen, G. Skaugen, T. V. Skiple, P. Neksa, and T. Andresen, "Development and Evaluation of a Reversible CO2 Residential Air Conditioning System Compared to a State-of-the-art R410A Unit," in *6th Gustav Lorentzen Conference on Natural Working Fluids*, Glasgow, Scotland, 2004.

[23] J. S. Brown, Y. Kim, and P. A. Domanski, "Evaluation of carbon dioxide as R-22 substitute for residential air-conditioning," *ASHRAE Trans.*, vol. 108 PART 2, pp. 954–963, 2002.

[24] D. M. Robinson and E. A. Groll, "Efficiencies of transcritical CO2 cycles with and without an expansion turbine," *Int. J. Refrig.*, vol. 21, no. 7, pp. 577–589, 1998.

[25] D. E. Boewe, C. W. Bullard, J. M. Yin, and P. S. Hrnjak, "Contribution of internal heat exchanger to transcritical R-744 cycle performance," *HVAC&R Res.*, vol. 7, no. 2, pp. 155–168, 2001.

[26] D. Li and E. A. Groll, "Transcritical CO2 refrigeration cycle with ejector-expansion device," *Int. J. Refrig.*, vol. 28, no. 5, pp. 766–773, 2005.

[27] S. Shet, O. Patil, and N. Agrawal, "Energetic and exergetic studies of modified CO2 transcritical refrigeration cycles," *Refrig. Sci. Technol.*, pp. 186–193, 2016.

[28] J. Stene, "Residential CO2 heat pump system for combined space heating and hot water heating," *Int. J. Refrig.*, 2005.

[29] H. Cho, C. Ryu, Y. Kim, and H. Y. Kim, "Effects of refrigerant charge amount on the performance of a transcritical CO2 heat pump," *Int. J. Refrig.*, vol. 28, no. 8, pp. 1266–1273, 2005.

[30] W. Marion and K. Urban, "User's Manual for TMY2s (Typical Meteorological Years) - Derived from the 1961-1990 National Solar Radiation Data Base. NREL Report No. TP-463-7668," http://rredc.nrel.gov/solar/#publications, 1995.

[31] ASHRAE, "ASHRAE Handbook: HVAC Applications," SI Edition., Amer. Soc. Heating, Ref. Air-Conditioning Eng. Inc.: Atlanta, GA, 2019.

[32] K. Hamanaka and K. Fujima, "Heat Pump Employing CO2 as Refrigerant and its Operating Method," European Patent EP1811246, 2007.

[33] P. X. Jiang, F. Z. Zhang, Y. W. Zhang, Y. S. Lin, and G. L. Wang, "Theoretical and experimental investigation of ground source CO2 heat pump and air conditioning systems, paper 424," in *UECTC'09 - Proceedings of 2009 US-EU-China Thermophysics Conference - Renewable Energy*, 2009.

[34] B. T. Austin and K. Sumathy, "Parametric study on the performance of a direct-expansion geothermal heat pump using carbon dioxide," *Appl. Therm. Eng.*, vol. 31, no. 17–18, pp. 3774–3782, 2011.

[35] P. Eslami-Nejad, M. Badache, A. Bastani, and Z. Aidoun, "Detailed theoretical characterization of a transcritical CO2 direct expansion ground source heat pump water heater," *Energies*, vol. 11, no. 2, 2018.

[36] P. Eslami-Nejad, M. Ouzzane, and Z. Aidoun, "A quasi-transient model of a transcritical carbon dioxide direct-expansion ground source heat pump for space and water heating," *Appl. Therm. Eng.*, vol. 91, pp. 259–269, 2015.

[37] H. Ghazizade-Ahsaee and M. Ameri, "Energy and exergy investigation of a carbon dioxide direct-expansion geothermal heat pump," *Appl. Therm. Eng.*, vol. 129, pp. 165–178, 2018.

[38] Z. Jin, T. M. Eikevik, P. Neksa, and A. Hafner, "A steady and quasi-steady state analysis on the CO2 hybrid ground-coupled heat pumping system," *Int. J. Refrig.*, vol. 76, pp. 29–41, 2017.

[39] ISO, "ISO 13256-1:1998 Standard for Water-source heat pumps -- Testing and rating for performance -- Part 1: Water-to-air and brine-to-air heat pumps." International Standards Organization, 1998.

[40] Waterfurnace, "Waterfurnace Specifications Catalog: 3-Series 300A11." 2018.

[41] C.F.R., *Energy efficiency standards and their compliance dates*. 10 CFR 431.97: United States Code of Federal Regulations, https://gov.ecfr.io/cgi-bin/ECFR, 2019.

[42] EnergyStar, "Energy Star Efficiency Requirements for Geothermal Heat Pumps," 2019. [Online]. Available: https://www.energystar.gov/products/heating_cooling/heat_pumps_geothermal/key_product_criteria. [Accessed: 01-Aug-2019].

[43] P. Kalinowski, D. Nasuta, C. Martin, and W. Hoffman, "Geothermal CO2 Air Conditioner

- Final Report to NIST, Solicitation # SB1341-15-RQ-0186," (not publically available), 2016.

[44] DIN, *DIN EN 12449: European Standard for Copper and copper alloys - seamless, round tubes for general purposes*. German Institute for Standardization (DIN): Berlin, Germany, https://www.din.de/en, 2016.

[45] ANSI/ASHRAE, *ANSI/ASHRAE Standard 37-2009: Method of Testing for Rating Electrically Driven Unitary Air-Conditioning and Heat Pump Equipment*. https://www.techstreet.com/standards/ashrae-37-2009?product_id=1650947, 2009.

[46] AMCA, *ANSI/AMCA 210-16, ANSI/ASHRAE 51-16: Laboratory Methods of Testing Fans Certified Aerodynamic Performance Rating*. Air Movement and Control Association International: Arlington Heights, IL, USA, http://www.amca.org/, 2016.

[47] Environol, "Environol Closed Loop Fluid Specification Catalog - Environol 1000 Concentration," http://www.waterfurnace.ca/Products/Accessories/environol.php, 2011.

[48] AHRI, *AHRI Standard 210/240: Performance Rating of Unitary Air-Conditioning & Air-Source Heat Pump Equipment*. Air-Conditioning Heating and Refrigeration Institute: Arlington, VA, 2017.

[49] S. A. Klein, *Engineering Equation Solver (EES), v. 10.667*. http://www.fchart.com/ees/, 2019.

[50] W. Span, R., Wagner, "A New Equation of State for Carbon Dioxide Covering the Fluid Region from the Triple-Point Temperature to 1100 K at Pressures up to 800 MPa," *Phys. Chem, Ref. Data*, vol. 25, no. 6, 1996.

[51] ASHRAE, *ASHRAE Handbook: HVAC Systems and Equipment*. Amer. Soc. Heating, Ref. Air-Conditoning Eng. Inc.: Atlanta, GA, 2016.

[52] Dorin, "Dorin CO2 Semi-Hermetic Compressors CD Series - Technical Specifications," http://www.dorin.com/, 2014.

[53] P. A. Domanski, D. A. Didion, and J. P. Doyle, "Evaluation of suction-line/liquid-line heat exchange in the refrigeration cycle," *Int. J. Refrig.*, vol. 17, no. 7, pp. 487–493, 1994.

[54] ASHRAE, *ASHRAE Handbook: Fundamentals*. Amer. Soc. Heating, Ref. Air-Conditioning Eng. Inc.: Atlanta, GA, 2017.

[55] ANSI/ASHRAE, "ANSI/ASHRAE Standard 206-2013: Method of Testing for Multipurpose Heat Pumps for Residential Space Conditioning and Water Heating." Amer. Soc. Heating, Ref. Air-Conditoning Eng. Inc., 2013.

[56] E. Balke, G. Nellis, S. Klein, H. Skye, V. Payne, and T. Ullah, "Detailed energy model of the National Institute of Standards and Technology Net-Zero Energy Residential Test Facility: Development, modification, and validation," *Sci. Technol. Built Environ.*, 2017.

[57] E. C. Balke, "Modeling, Validation, and Evaluation of the NIST Net Zero Energy Residential Test Facility," Master's Thesis, University of Wisconsin - Madison, https://sel.me.wisc.edu/publications-theses.shtml, 2016.

[58] W. Wu, H. M. Skye, and P. A. Domanski, "Selecting HVAC systems to achieve comfortable and cost-effective residential net-zero energy buildings," *Appl. Energy*, vol.

212, pp. 577–591, 2018.

[59] UNS, *Metals and Alloys in the Unified Numbering System (UNS), DS56L-EB,* 13th ed. ASTM International: West Conshohocken, PA, USA, https://www.astm.org, 2017.

[60] A. Hayes, N., Jokar, “Dynalene/Water Correlations to Be Used for Condensation of CO2 in Brazed Plate Heat Exchangers,” *ASHRAE Trans.*, vol. 115, no. 2, 2009.

8 Figures

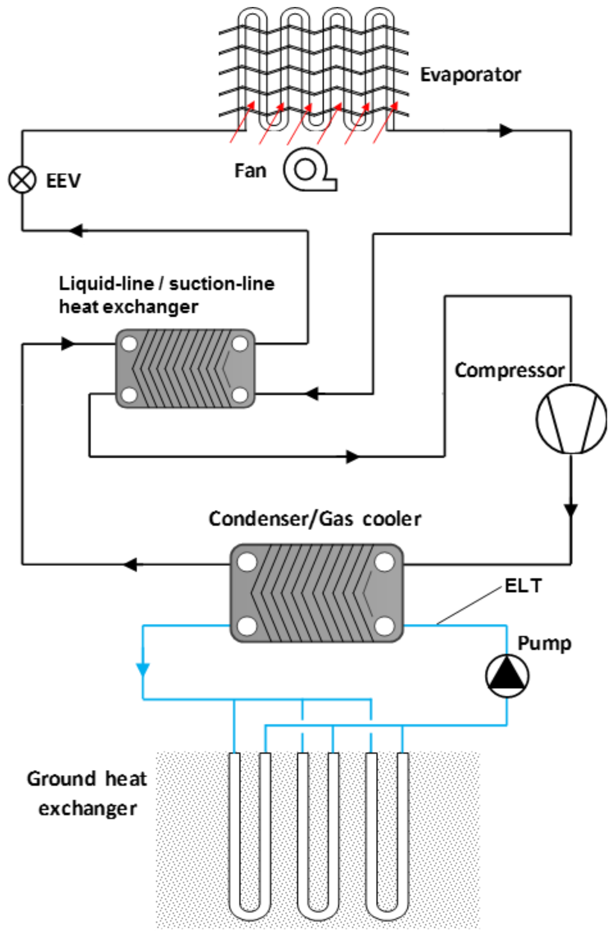

Fig. 1: Schematic of the tested liquid-to-air CO_2 GSAC connected to a GSHX

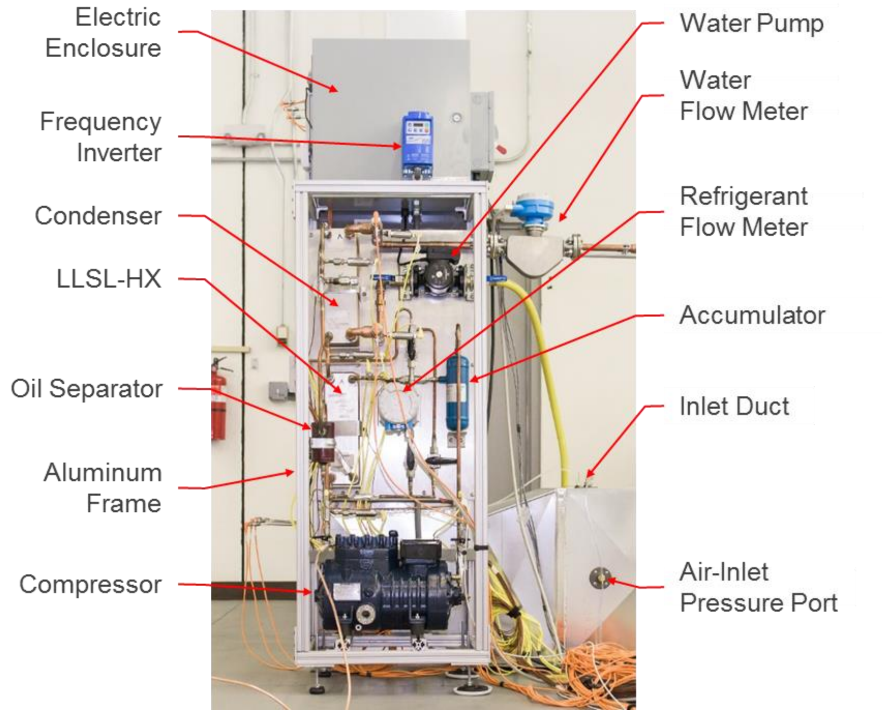

(a) Unit components attached to aluminum frame

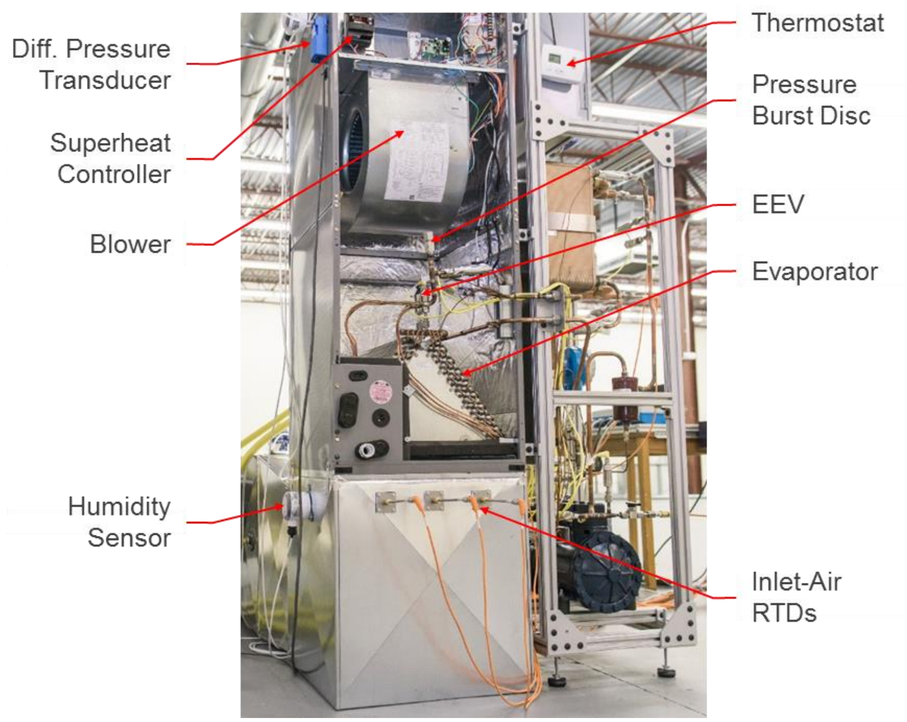

(b) Modified air handler

Fig. 2: Photograph of the tested liquid-to-air CO_2 GSAC

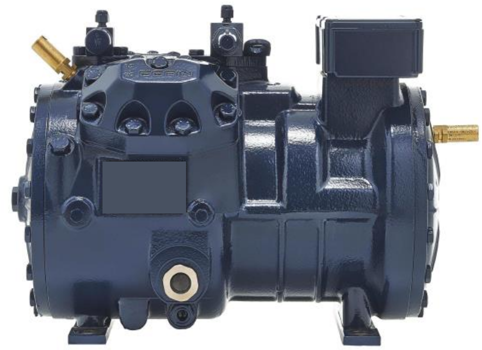

(a) Semi-hermetic reciprocating compressor

(c) Plate heat exchanger

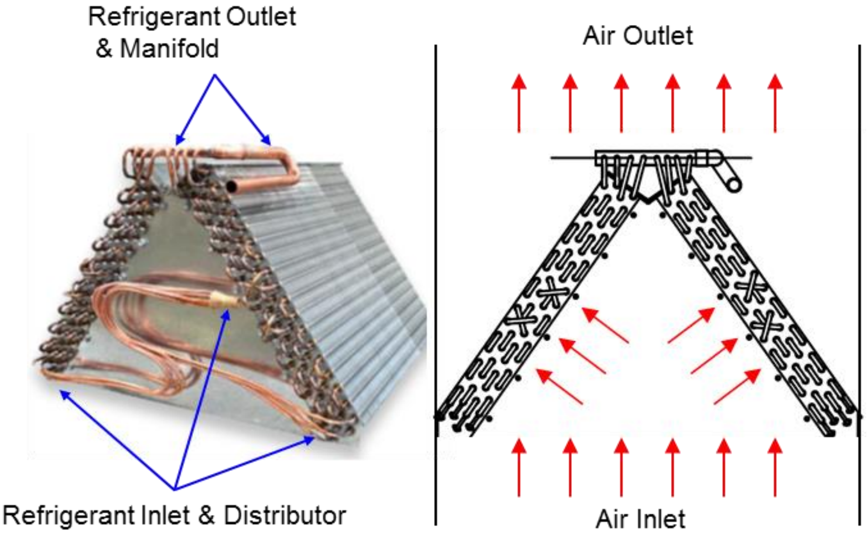

(b) Fin-tube heat exchanger

Fig. 3: Main components of the tested liquid-to-air CO_2 GSAC

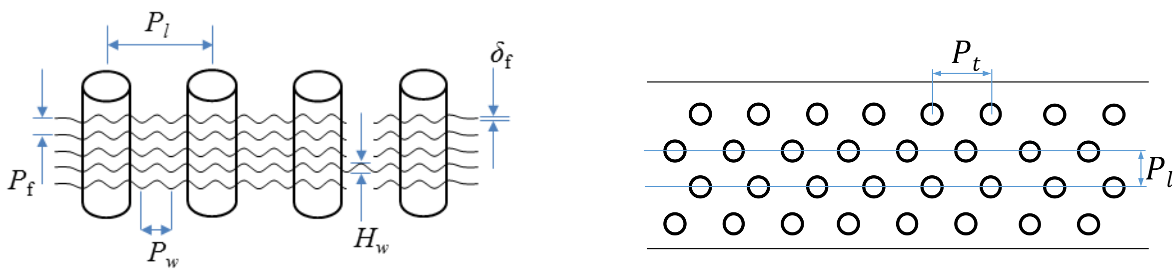

(a) Top view

(b) Side view

Fig. 4: Geometry of the A-frame wavy fin-tube heat exchanger

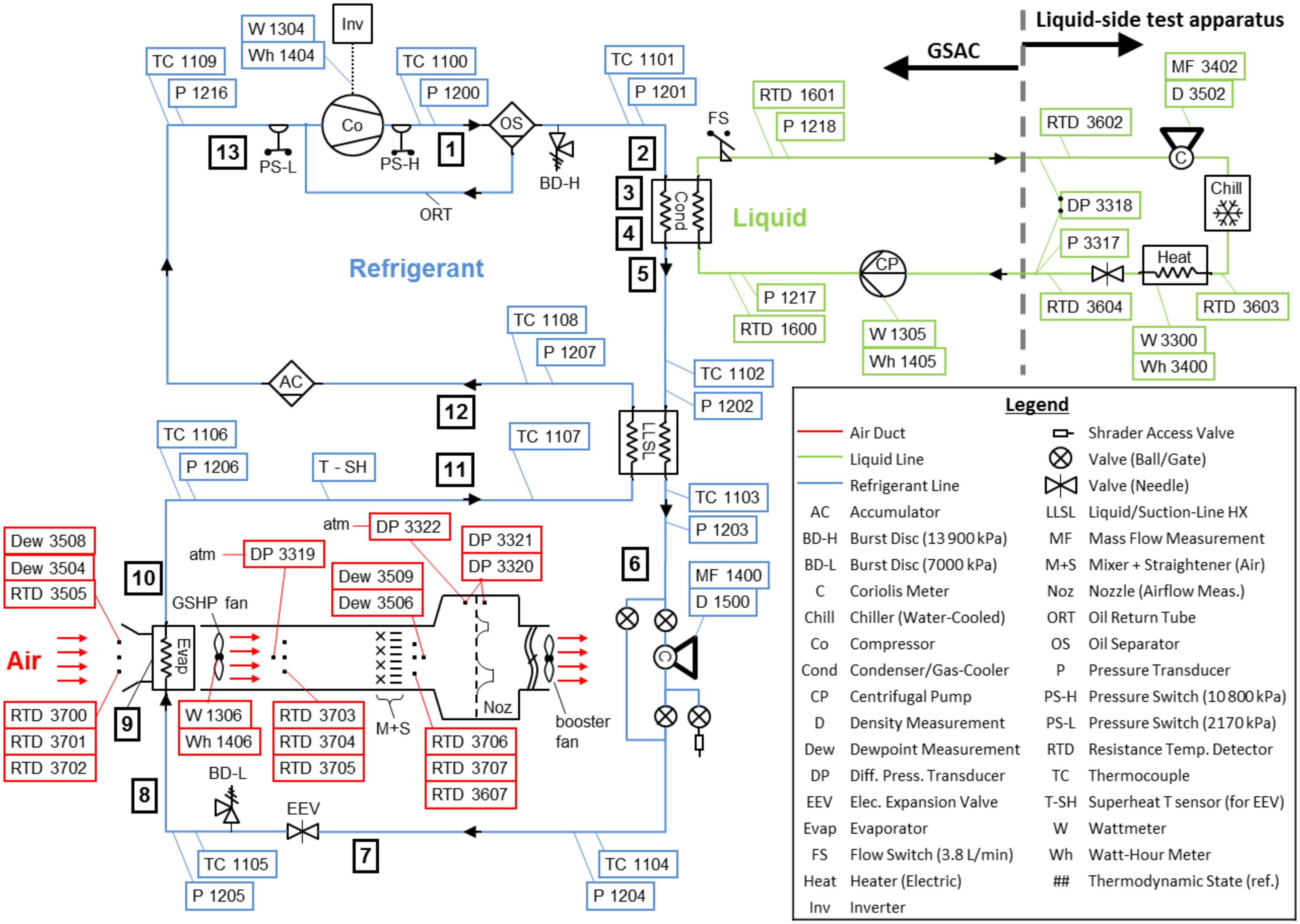

Fig. 5: Instrumentation for the CO_2 GSAC

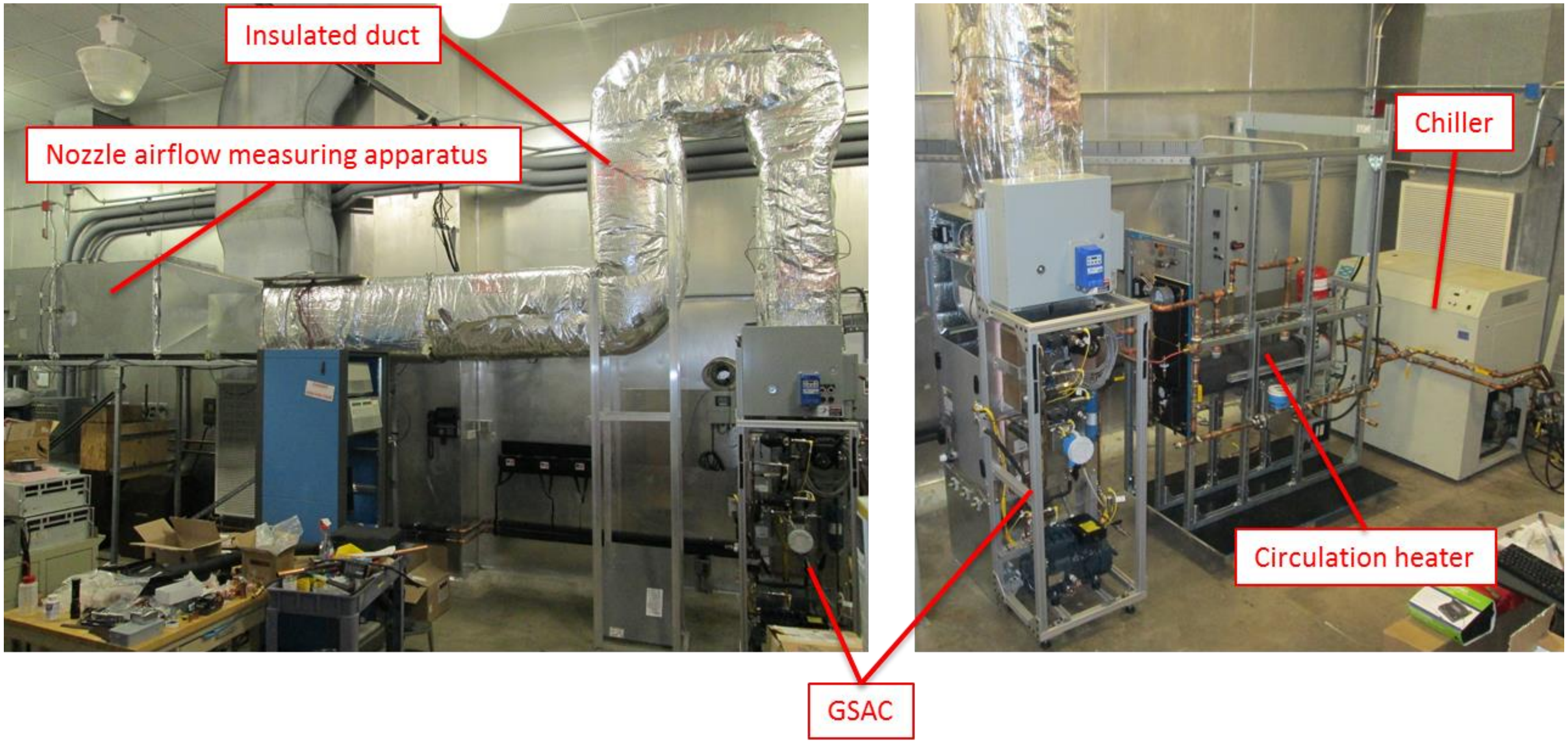

Fig. 6: GSAC test apparatus inside the environmental chamber

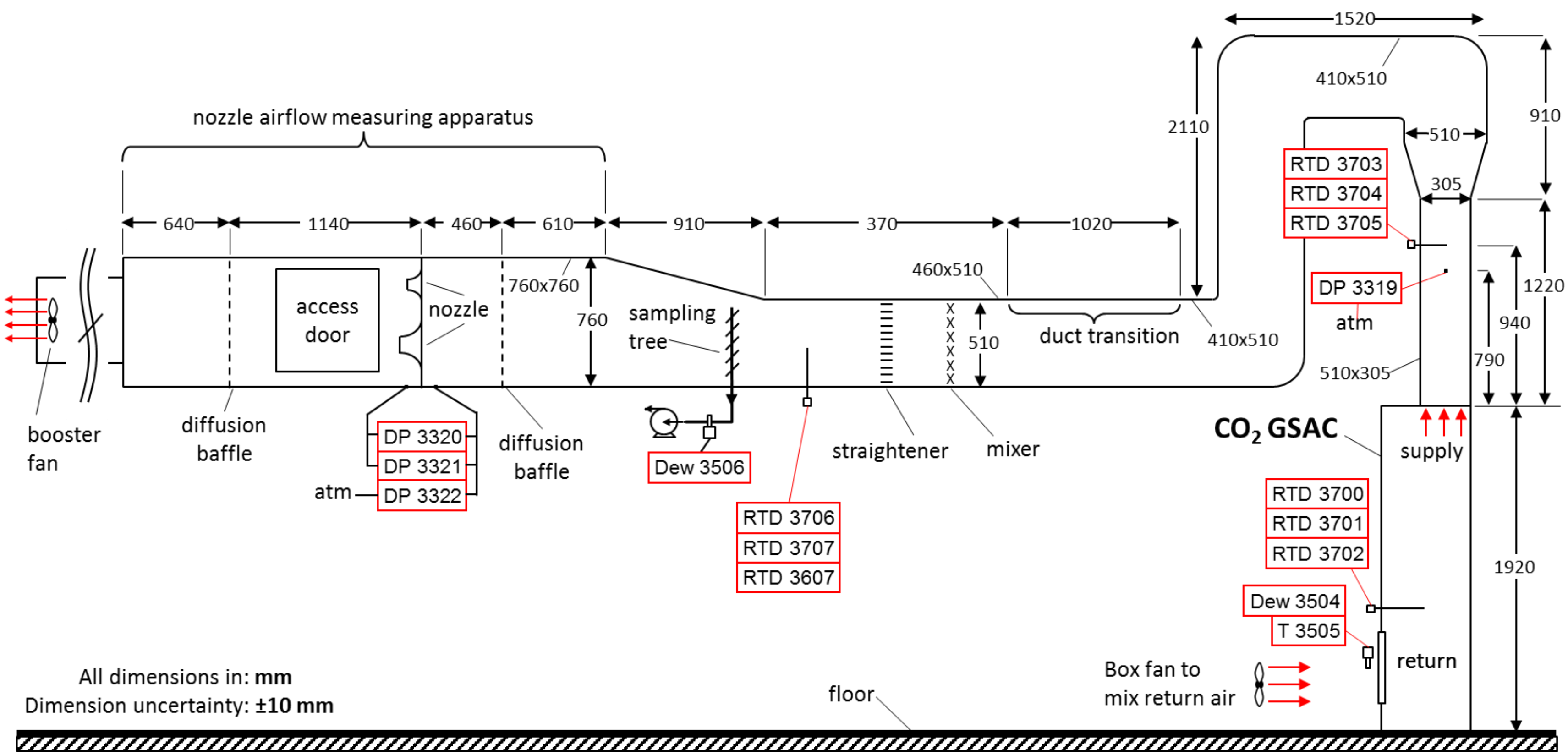

Fig. 7: Air-side measurement apparatus

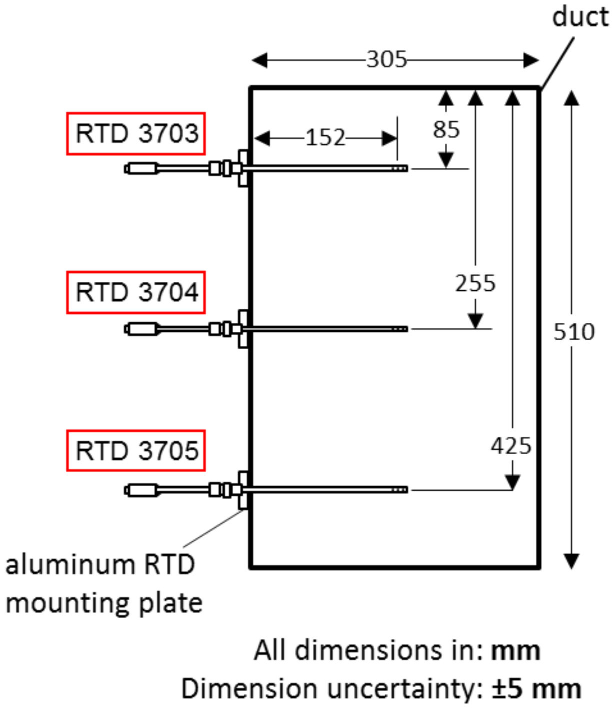

(a) Duct-mount RTD

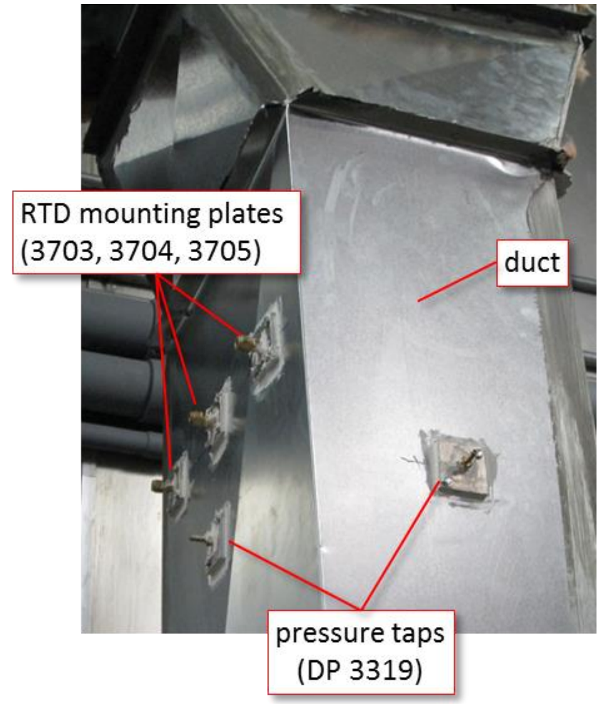

(b) RTDs and pressure taps

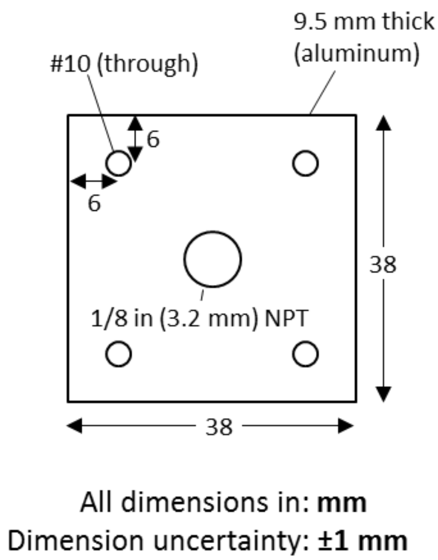

(c) Mounting plate for RTDs and pressure taps

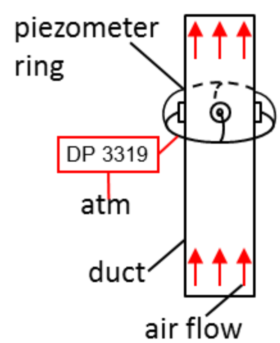

(d) Piezometer ring for pressure measurement

Fig. 8: Air-side RTD and pressure tap details

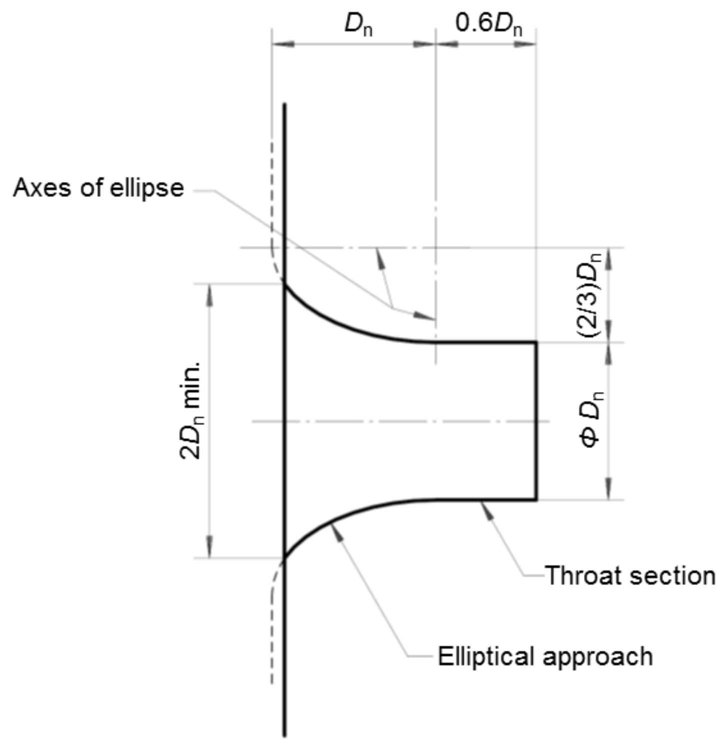

Fig. 9: Nozzle dimensions, per ANSI/AMCA 210-16 (ANSI/ASHRAE 51-16) standard

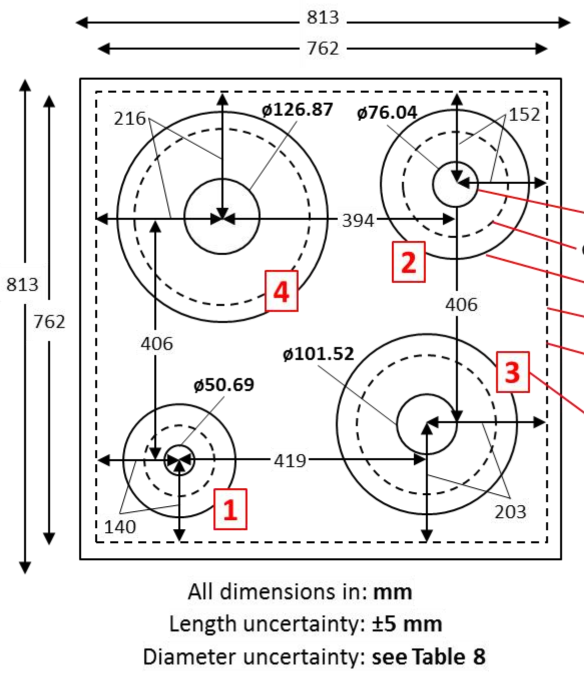

(a) Dimensions

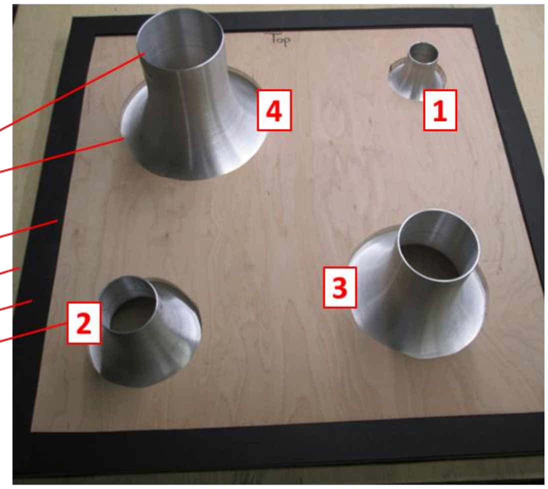

(b) Front side

(c) Back side, with counterbore

(d) Back side, with nozzles

(e) Installed in duct

Fig. 10: Airflow measurement nozzle board

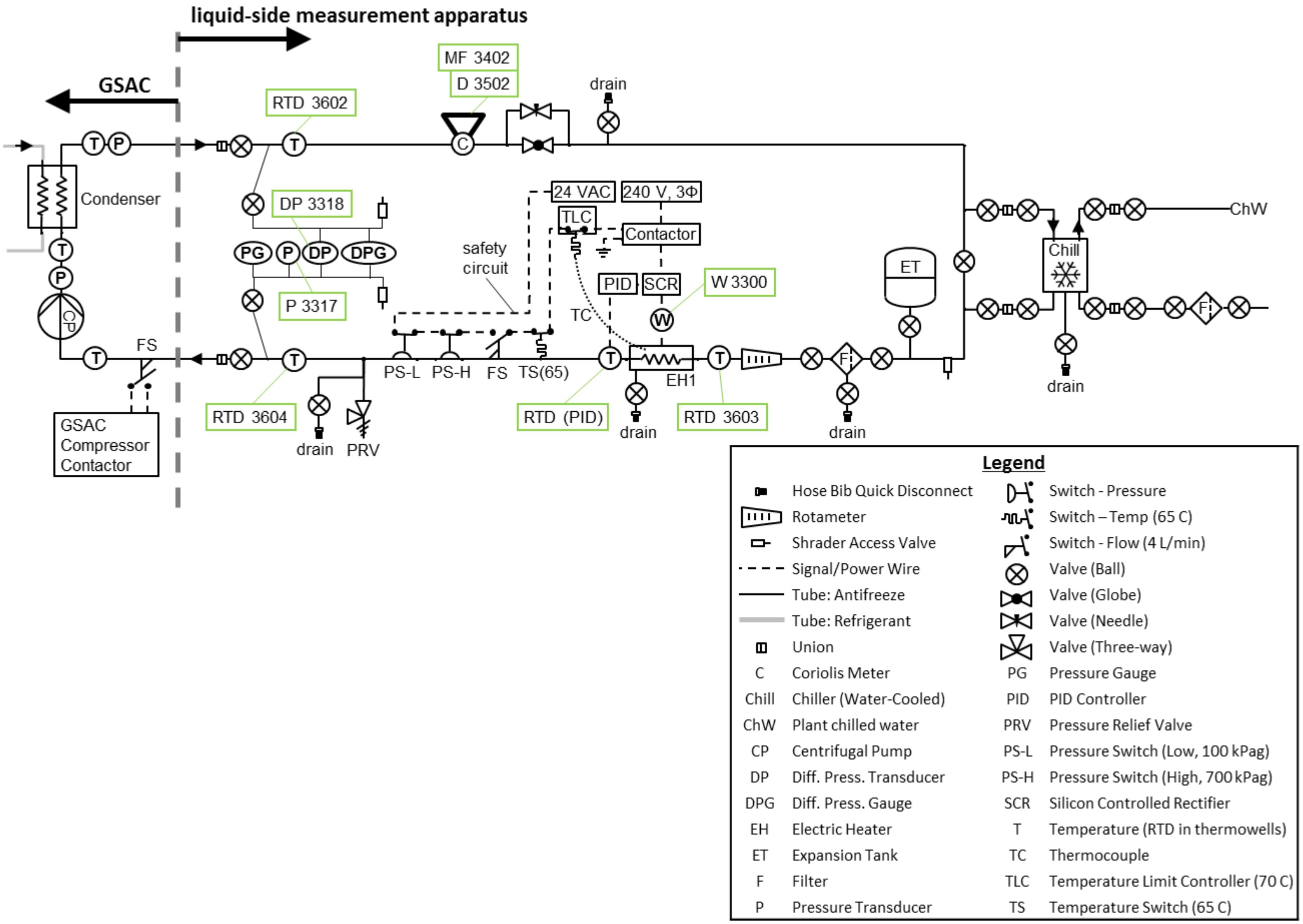

Fig. 11: Liquid-side measurement apparatus

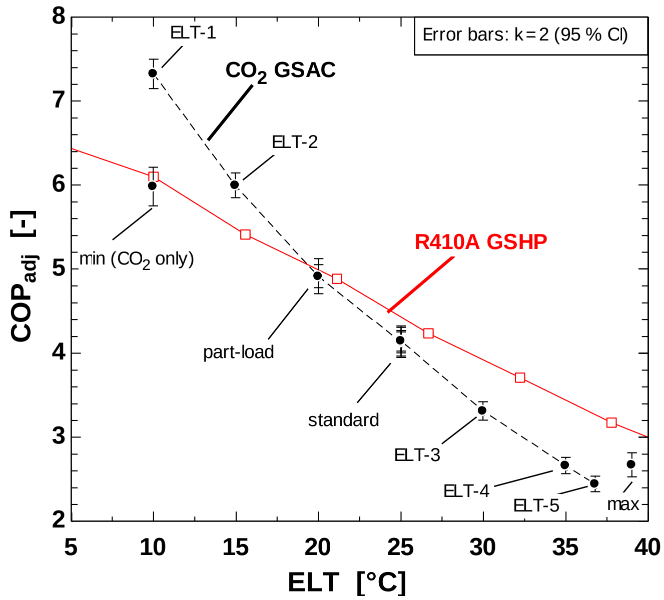

(a) Coefficient of performance

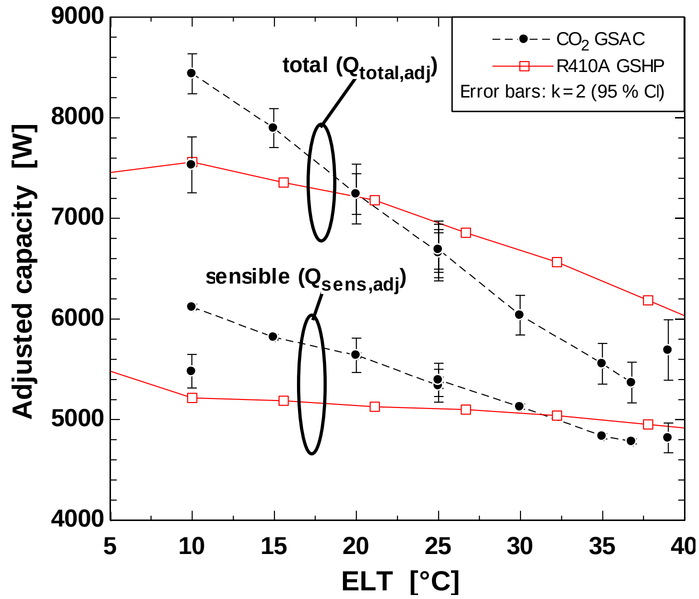

(b) Capacity

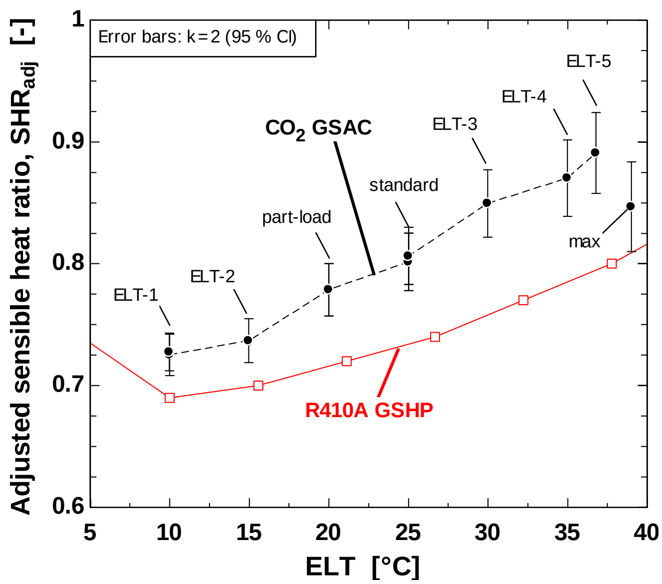

(c) Sensible heat ratio

Fig. 12: Comparison of CO2 GSAC with commercially-available R410A GSHP.

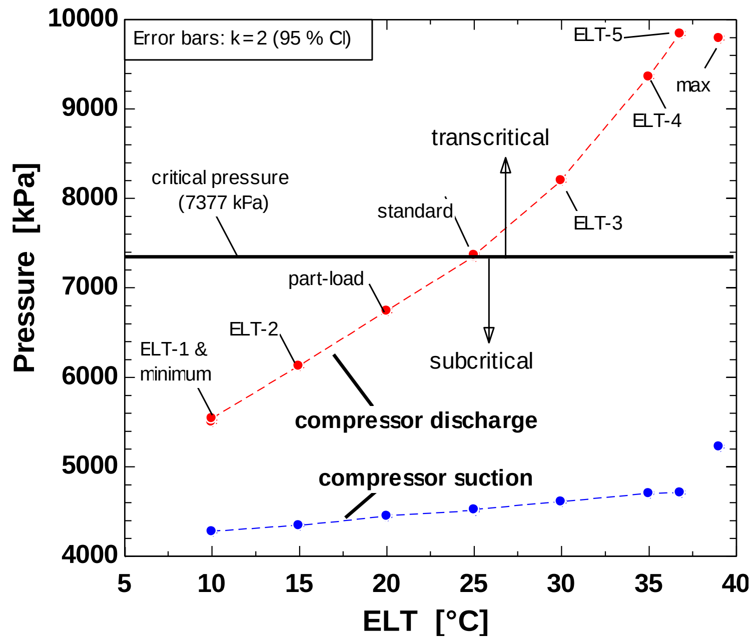

Fig. 13: Compressor suction and discharge pressures

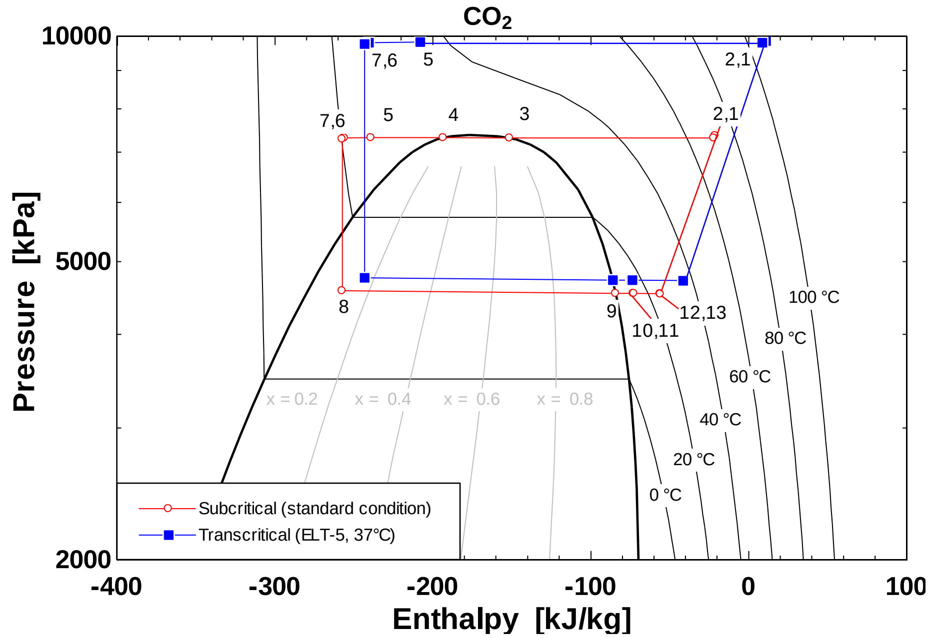

(a) P-h diagram: Tested CO_2 GSAC (with LLSL-HX)

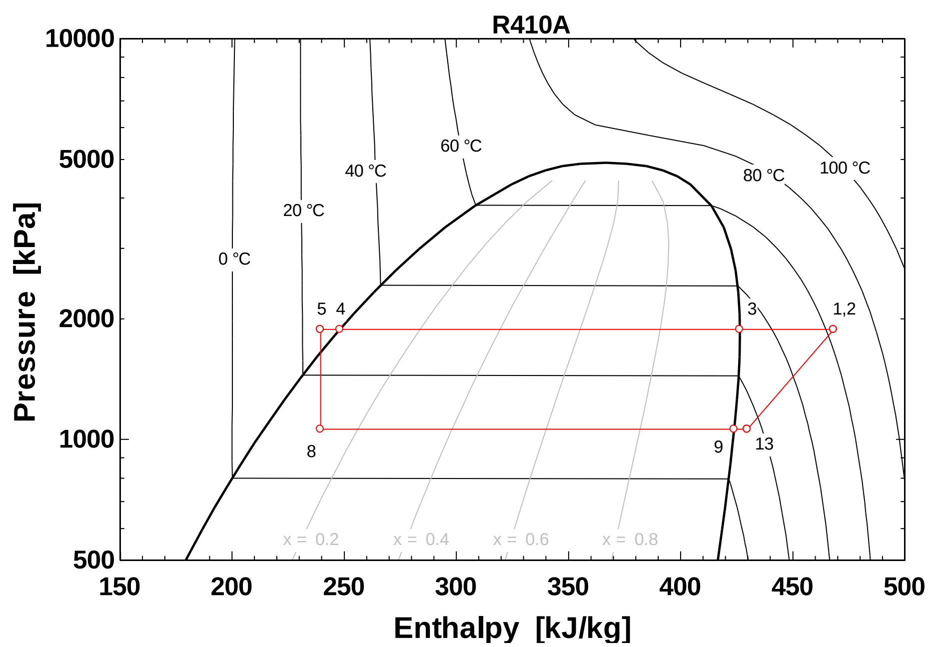

(b) P-h diagram: Conventional R410A GSHP at 'standard' condition (no LLSL-HX)

Fig. 14: Pressure-enthalpy diagrams

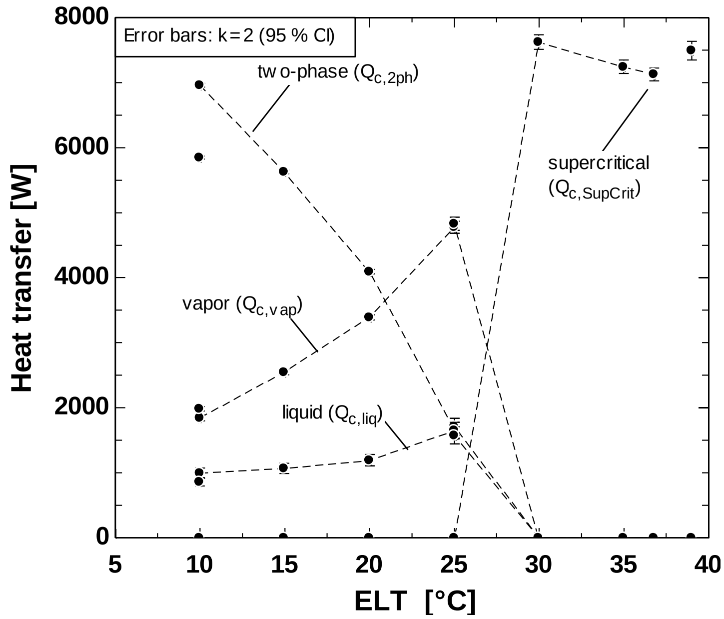

Fig. 15: Heat transfer in condenser/gas-cooler, divided by refrigerant phase

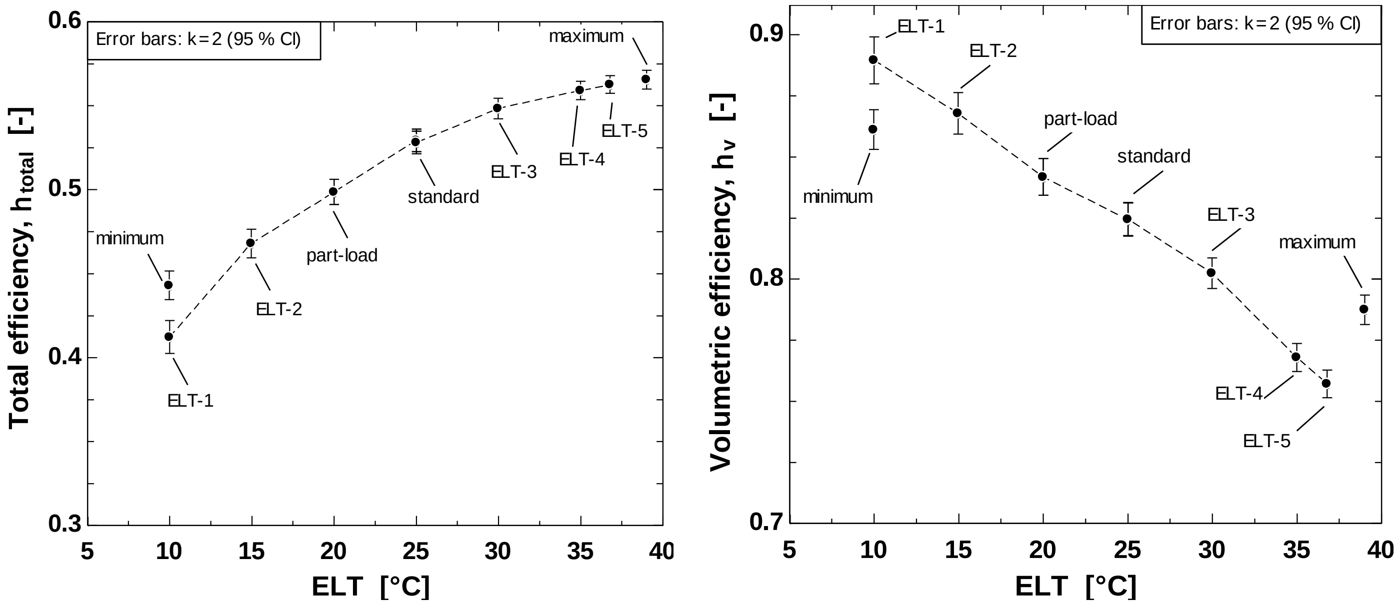

(a) Total efficiency (b) Volumetric efficiency

Fig. 16: Compressor efficiency

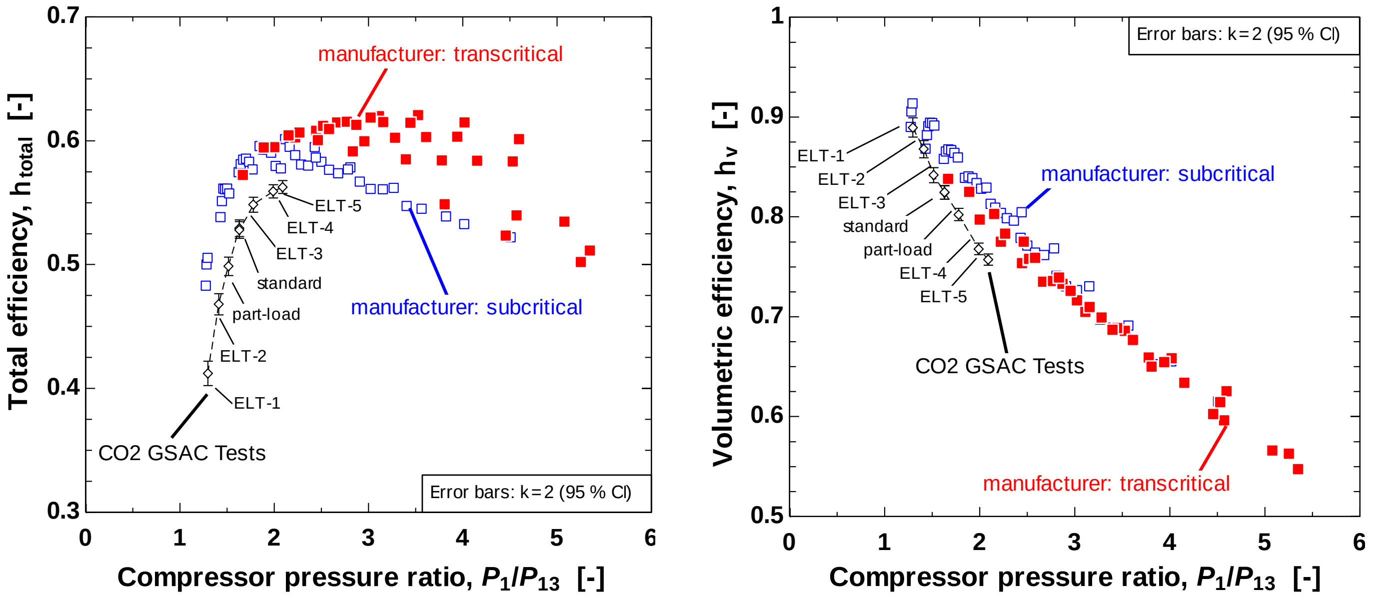

(a) Total efficiency (b) Volumetric efficiency

Fig. 17: Compressor efficiency: comparison of measurements and manufacturer's data

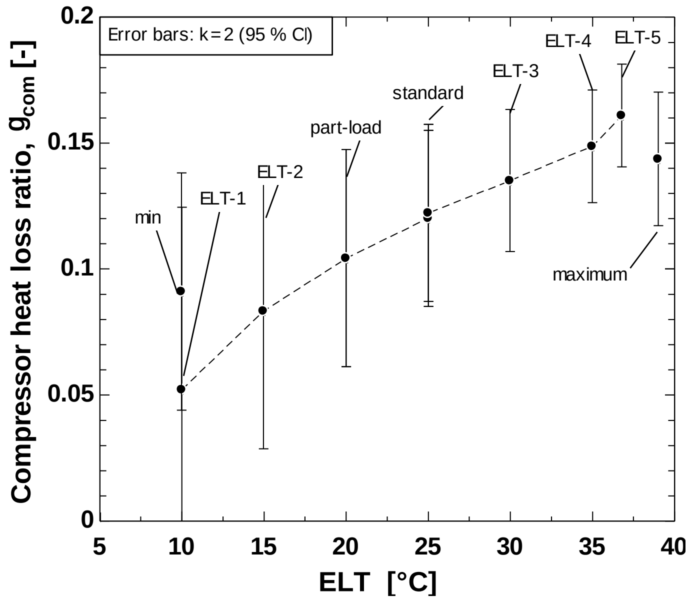

Fig. 18: Compressor heat-loss ratio

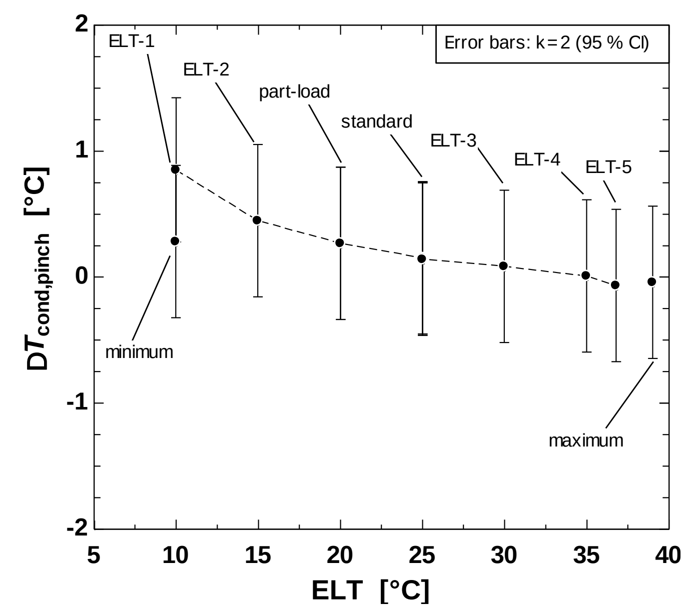

Fig. 19: Condenser pinch-point temperature

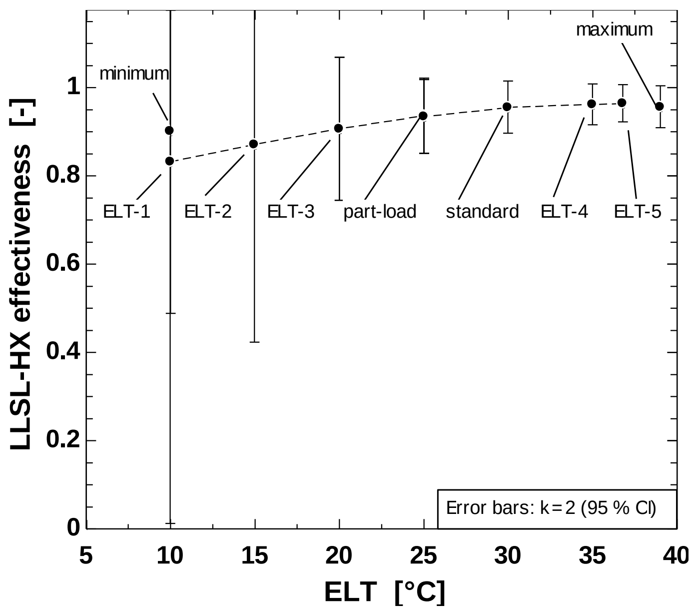

Fig. 20: LLSL-HX effectiveness

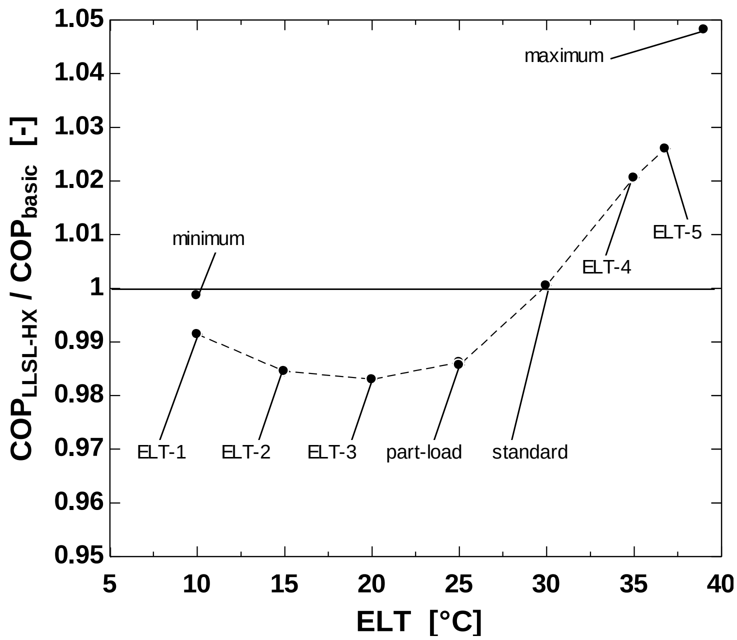

Fig. 21: Estimated COP with and without the LLSL-HX

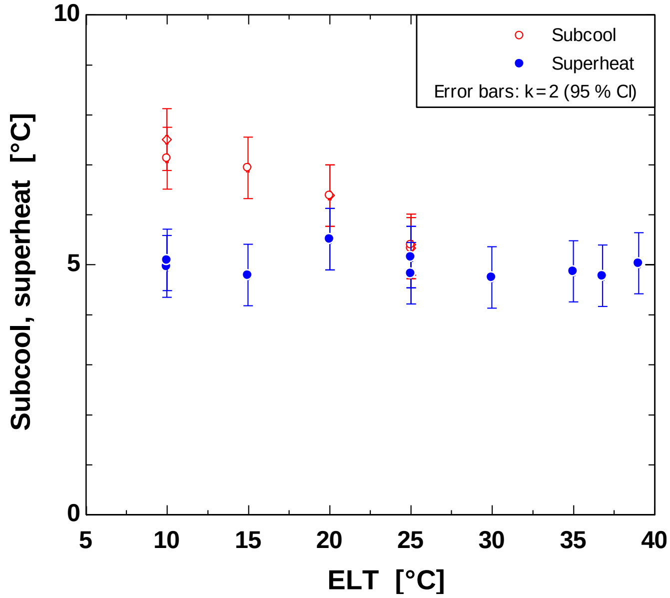

Fig. 22: Evaporator-exit superheat and condenser-exit subcooling

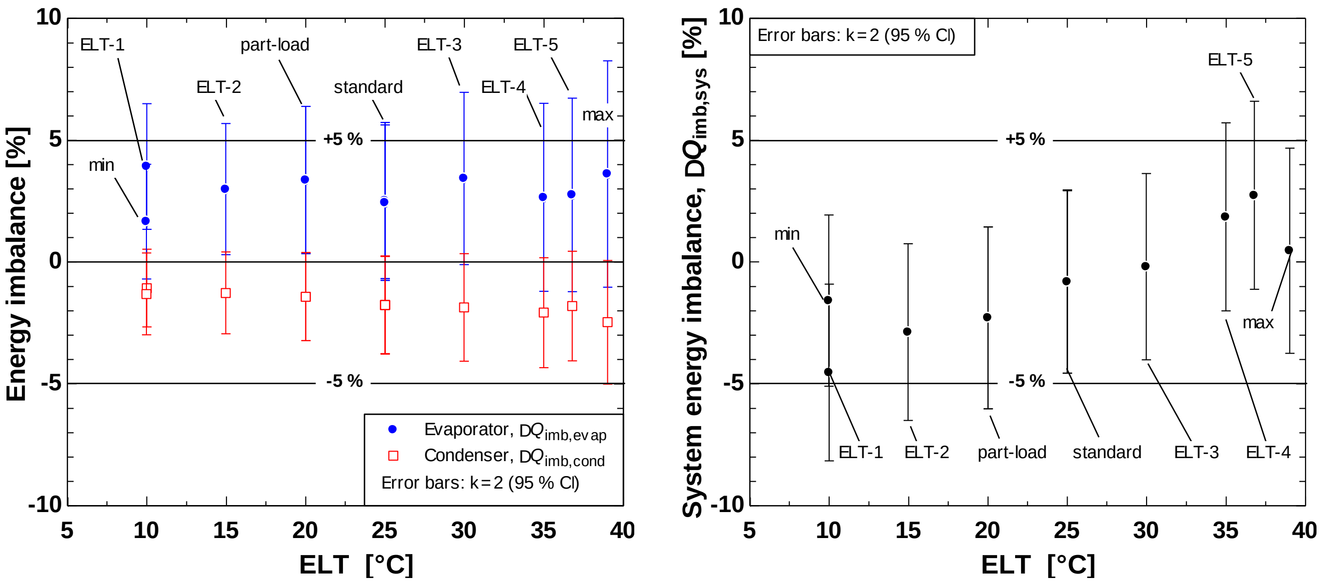

(a) Condenser/gas-cooler and evaporator (b) Entire GSAC system

Fig. 23: Imbalance of measured energy transfers

9 Tables

Table 1: Main components of the CO_2 GSAC, including MAWP

Component	Parameter	Value	MAWP[1]
Accumulator	Type:	Suction-line acumen. for transcritical CO_2 systems	10 000 kPa
Air Handler	Airflow range: Electrical input: Insulation: Nominal capacity: Blower motor type:	208-1400 L/s 208/230 V 1Φ 60 Hz R-value 0.74 K·m^2/W (4.2 °F·ft^2/Btu) 14.1 kW (4 tons) Electronically commutated	N/A
Burst discs	Burst pressure: Type:	13 800 kPa (high), 6900 kPa (low) 8.3 mm angled seat, 316 stainless steel	N/A
Compressor	Type:	Semi-hermetic reciprocating (Table 2)	17 000 kPa
Condenser/gas-cooler	Type:	Brazed-plate, corrugated channels (Table 4)	14 000 kPa
EEV (PWM)	Type: Rated Capacity: Pressure rating: PWM time period:	Pulse-width modulation (PWM) 6.7 kW (1.9 tons) Higher max open press. diff. (MOPD) 3 s	12 000 kPa[2]
Evaporator	Configuration:	A-frame, wavy fin-tube (Table 3)	7000 kPa
Fittings	Material:	Copper-iron alloy, 97.5 % Cu, 2.4 % Fe, 0.13 % Zn, 0.03 % P, per UNS C19400 [59]	12 000 kPa
Inverter for Compressor	Electrical in/out: Maximum power:	Converts 240 V 1Φ to 240 V 3Φ 2.2 kW, 17.1 A (input) and 9.6 A (output)	N/A
LLSL-HX	Type:	Brazed-plate, corrugated channels (Table 4)	14 000 kPa
Oil separator	Type: Efficiency: Connection size: Maximum capacity:	Coalescing, hermetic 98 % 6.3 mm (0.25 in) 19.6 kW @ 37.8 °C gas-cooler outlet, 5.6 °C superheat, 0 °C subcooling)	13 000 kPa
Pressure switch (high)	Setpoint:	10 700 kPa	35 000 kPa
Pressure switch (low)	Setpoint:	2070 kPa	35 000 kPa
Pump (GSHX fluid)	Type: Electrical input: Flow range: Head range: Nominal power:	Variable-speed circulator 115 V 1Φ 60 Hz (0 to 6.4) m^3/h (0 to 9.1) m 205 W	1000 kPa
Safety Head (for burst disc)	Orifice size: Tubing size:	5.6 mm 9.5 mm	138 000 kPa
Superheat Controller	Config:	Coupled with PWM-style EEV	N/A
Tubes	Manuf. Standard: Alloy: Constituents:	DIN EN 12499 [44] Copper-iron alloy, CuFe2P Fe (2.1 to 2.6) %, Zn (0.05 to 0.2) %, P (0.015 to 0.15) %, Pb maximum 0.03 %, balance is Cu	12 000 kPa

[1] Maximum allowable working pressure.

[2] Manufacturer's MAWP for stock expansion valve is 9000 kPa, where the connection tubes limit the pressure. This valve was modified with $CuFe_2P$ alloy tubes to increase the expected MAWP to 12 000 kPa.

Table 2: Specifications of the semi-hermetic reciprocating compressor

Parameter	Value
No. cylinders, N_{cyl}	2
Bore diameter, D_b (mm)	22
Stroke, L_s (mm)	22
Displacement @ 50Hz (m^3/h)	1.46
Speed @ 50Hz (RPM)	1450
Suction valve (mm)	10
Discharge valve (mm)	14
Oil Type and charge (kg)	Polyolester (POE), 1.3
Oil kinematic viscosity (mm^2/s)	80 @ 40 °C, 10.6 @ 100 °C
Net weight (kg)	73

Table 3: Specifications of the A-frame wavy fin-tube evaporator

Parameter	Value
Number of slabs	2
Number of columns	16
Number of rows	4
Tube material	copper
Tube length (mm)	457
Tube inner surface	rifled
Tube rifling fin height (mm)	0.076
Tube outside diameter, D_o (mm)	5.0
Tube inside diameter (fin root diameter), D_i (mm)	4.59
Tube wall thickness (mm)	0.21
Transverse tube pitch, P_t (mm)	19
Longitudinal tube pitch, P_l (mm)	11
Fin material	aluminum
Fin pitch, P_f (mm)	1.59
Fin thickness, δ_f (mm)	0.14
Fin length, L_f (mm)	44
Fin enhancement	sine wave
Fin wave pitch, P_w (mm)	3.2
Fin wave height (peak-to-peak), H_w (mm)	0.87

Table 4: Specifications of the PHXs for the condenser/gas-cooler and the LLSL-HX

Parameter	Small PHX	Large PHX
Number of plates, N_p	10	76
Plate length (mm)	377	377
Fluid flow plate length, L_p (mm)	311	311
Plate width, w_p (mm)	119.5	119.5
Fluid flow plate area, $A_p = (N_p - 2)\cdot L_p\cdot w_p$ (m^2)	0.2973	2.75
Plate thickness (mm)* [60]	0.4	0.4
Mean channel spacing (mm)* [60]	2	2
Enlargement factor	1.1	1.1
Port diameter (mm)	27	27
Surface enhancement	chevron**	chevron**

* The plate thickness and channel spacing were taken from [60] as representative values

**The details of the chevron enhancement are not known.

Table 5: Dimensions of the connection tubes and auxiliary components

Description	Length/height (mm)	Diameter (mm)	Thickness (mm)	Volume (cm^3)
Tube: compressor to oil separator	777.9	12.8	0.4	87.98
Tube: oil separator to condenser	863.6	12.8	0.4	97.67
Tube: condenser to LLSL-HX	469.9	12.8	0.4	53.14
Tube: LLSL-HX to EEV	2044.7	9.5	0.4	121.55
Tube: flow meter bypass	822.3	9.5	0.4	48.88
Tube: EEV to evaporator	342.9	9.5	0.4	20.38
Tube: evaporator to LLSL-HX	1609.7	12.8	0.4	182.05
Tube: LLSL-HX to accumulator	444.5	12.8	0.4	50.27
Tube: accumulator to compressor	1104.9	12.8	0.4	124.96
Oil separator	120.0	73.0*	-	491.30*
Accumulator	250.0	76.1 (OD)	-	800**

*Oil separator outer diameter and volume, since wall thickness is not known

**Accumulator internal volume from manufacturer's specifications

Table 6: Instruments and uncertainties

Location	Transducer	Unit	±Uncertainty[1]	Req'd. ±Uncertainty[2]
Refrigerant	Thermocouple	°C	0.6	N.A.
Refrigerant	Pressure	kPa	20	N.A.
Refrigerant	Coriolis – mass flow	g/s	0.25 %	N.A.
Refrigerant	Coriolis – density	kg/m^3	20	N.A.
Air	RTD	°C	0.075	0.2
Air	Dew-point[3]	°C	0.25	0.37[3]
Air	Differential Pressure	Pa	2	5
Air	Airflow[4]	L/s	3 %	N.A.
Liquid	RTD	°C	0.075	0.1
Liquid	Differential Pressure	kPa	0.1 (≈0.5%)	5 %
Liquid	Pressure	kPa	1	N.A.
Liquid	Coriolis – mass flow	g/s	0.25 %	5 %
Liquid	Coriolis – density	kg/m^3	0.5	N.A.
Electrical	Power	W	0.2 %	0.5 %
Electrical	Energy	Wh	0.2 %	0.5 %

[1]All uncertainties are for a 95 % confidence interval (k = 2)

[2]Maximum sensor uncertainty level specified in Table 8 of ISO 13256-1 [39]

[3]Table 8 of ISO 13256-1 [39] specified maximum uncertainty of wet-bulb temperature measurement of ±0.2 °C. At 27 °C dry-bulb temperature, the derivative of dew-point temperature w/ respect to wet-bulb temperature is 1.87. Therefore, the required uncertainty of dewpoint measurement is = 0.2 °C * 1.87 = 0.37 °C

[4]A ±3 % uncertainty was added to the airflow measurement, in addition to the instrument uncertainty, based on comparative tests with a venturi flowmeter with a ±1 % uncertainty

Table 7: Test apparatus equipment

Component	Parameter	Value
		Air-side components
Air sample module	Flowrate:	(0 to 2.5) L/min
Air sample filter	Shell: Filter type: Filter efficiency: Filter material:	Polycarbonate Coalescing 93 % efficient for 0.01 micron particles and droplets Borosilicate glass microfibers with fluorocarbon resin binders
Flow nozzles	Material: Dimensions: Manuf. Standard:	Spun aluminum See Table 8 ANSI/AMCA 210-16 (ANSI/ASHAE 51-16) [46]
		Liquid-side components
Chiller	Cooling Capacity: Reservoir volume: Stability:	25 kW @ 20 °C 151 L ±0.1 °C
Circulation heater	Electric input: Heating elements: High-limit sensor:	240 V, 3Φ, 24 kW 7 W/cm^2 Heater-sheath mounted type-J thermocouple
Circulation heater temp. limit controller	Heater-sheath temp. limit:	70 °C
Expansion tank	Size:	8 L (4 L acceptance volume)
Filter housing	Material: Size:	304L stainless steel 110 mm diameter, 250 mm height
Filter	Style: Material:	Cartridge Polypropylene string-wound sediment filter, 50 µm
Flow switch	Type:	Shuttle, set to 3.8 L/min
HTF needle valve	Type: Full-flow Cv:	Integral-bonnet with regulating stem 1.8
Press. relief valve	Material: Range:	Brass (0 to 2100(kPaG, set to 700 kPaG
Press. switch (high)	Type: Range:	Miniature watertight switch (170 to 700) kPaG, set to 700 kPaG
Press. switch (low)	Type: Range:	Miniature watertight switch (6 to 200) kPaG, set to 100 kPaG
Rotameter	Flow Range: Material: Pipe connections:	(3.8 to 38) L/min Polysulfone Sweat, 1.9 cm
SCR Power controller	Type: Electrical input:	Phase-angle fired (200 to 480) VAC, 3Φ/3-leg, 90A
Temperature switch	Range:	(20 to 95) °C, set to 65 °C
Thermowell	Size: Material:	Length: 19.1 cm, Sensor diameter: 1.3 cm 304 stainless steel
Transformer	Electrical in/out:	208 VAC 3Φ to 24 VAC 1Φ

Table 8: Airflow nozzles dimensions

Nozzle #	Thickness (mm)	Throat Diameter (mm)	Diameter Uncertainty (mm)	Area (mm^2)
1	3.2	50.69	0.039	2018
2	3.2	76.04	0.069	4541
3	3.2	101.52	0.064	8095
4	3.2	126.87	0.048	12643

Nozzles were fabricated according to the ANSI/AMCA 210-16, ANSI/ASHRAE 51-16 standard [46]

Table 9: Properties of the antifreeze HTF: water/ethanol/isopropanol 70/25/5 % (by mass)

Temperature (°C)	Specific heat (kJ/kg·K)	Density (kg/m3)	Thermal conductivity (W/m·K)	Dynamic viscosity (kg/m·s)
0	4380	981	0.47	4.98E-03
5	4384	981	0.47	3.76E-03
10	4388	981	0.48	3.00E-03
15	4391	981	0.48	2.51E-03
20	4395	981	0.49	2.13E-03
25	4399	981	0.49	1.82E-03
30	4403	981	0.50	1.57E-03
35	4406	981	0.51	1.40E-03
40	4410	981	0.51	1.26E-03
45	4414	981	0.52	1.11E-03
50	4417	981	0.52	9.58E-04

Data from HTF manufacturer [47]

Table 10: ISO 13256-1 standard test conditions

	Standard[1]	Part-Load[1]	Maximum[2]	Minimum[3]
Return air dry-bulb (°C)	27	27	32	21
Return air dew-point (°C)	14.7	14.7	19.2	11.0
Return air wet-bulb[4] (°C)	19	19	23	15
Airflow rate (L/s)	342			
Air surrounding unit dry-bulb (°C)	27	27	32	21
Entering liquid temperature (°C)	25	20	39[5]	10
Liquid flow rate (L/s)	0.2839			
Compressor frequency (Hz)	50			
Supply static pressure (Pa)	58			

[1]Reference: Table 1 in ISO 13256-1 [39].

[2]Reference: Table 3 in ISO 13256-1 [39].

[3]Reference: Table 5 in ISO 13256-1 [39].

[4]The wet-bulb temperature is specified in the ISO 13256-1 standard, but dew-point was used primarily here for convenience, since it was the native measure of the dew-point transmitters.

[5]An ELT of 39 °C was used because the 40 °C ELT specified by ISO 13256-1 for the 'maximum' test caused the high-side pressures to exceed the pressure transducer measurement limit of 10 000 kPa.

Table 11: 'Extended-ELT' test conditions

	ELT-1	ELT-2	ELT-3	ELT-4	ELT-5
Return air dry-bulb (°C)	27				
Return air dew-point (°C)	14.7				
Return air wet-bulb (°C)	19				
Airflow rate (L/s)	342				
Air surrounding unit dry-bulb (°C)	27				
Entering liquid temperature (°C)	10	15	30	35	36.8[1]
Liquid flow rate (L/s)	0.2839				
Compressor frequency (Hz)	50				
Supply static pressure (Pa)	58				

Reference: Table 1 in ISO 13256-1 [39]

[1]The highest ELT for the 'Extended ELT' tests was 36.8 °C because higher temperatures caused the high-side pressures to exceed the pressure transducer measurement limit of 10 000 kPa.

Table 12: Test tolerances

	Maximum variation	Variation of average from specified test target
Return air dry-bulb (°C)	± 1.0	± 0.3
Return air dew-point (°C)	± 0.9	± 0.6
Return air wet-bulb (°C)	± 0.5	± 0.2
Airflow rate (L/s)	± 10 % (± 30 L/s)	± 5 % (± 15 L/s)
Entering liquid temperature (°C)	± 0.5	± 0.2
Liquid flow rate (L/s)	± 2 % (± 0.006 L/s)	± 1 % (± 0.003 L/s)
Supply static pressure (Pa)	± 10 % (± 4 Pa)	± 5 % (± 2 Pa)

Reference: Table 9 in ISO 13256-1 [39]

Table 13: **Measurements and equations used to define refrigerant thermodynamic states**

State	Description	Measurements	Equations
1	Compressor discharge	TC 1100, P 1200	
2	Condenser inlet	TC 1101, P 1201	
3	Condenser saturated vapor	P 1201	$x_3 = 1$
4	Condenser saturated liquid	P 1202	$x_4 = 0$
5	Condenser outlet, LLSL-HX liquid inlet	TC 1102, P 1202	
6	LLSL-HX liquid outlet	TC 1103, P 1203	
7	Expansion valve inlet	TC 1104, P 1204	
8	Expansion valve outlet, Evaporator inlet	P 1205	$i_8 = i_7$
9	Evaporator saturated vapor	P 1206	$x_9 = 1$
10	Evaporator outlet	TC 1106, P 1206	
11	LLSL-HX vapor inlet	TC 1107, P 1206	
12	LLSL-HX vapor outlet	TC 1108, P 1207	
13	Compressor inlet	TC 1109, P 1206	

i = enthalpy, x = thermodynamic vapor quality

Appendix A: Data

The raw measurements (Table A-1) and calculated performance metrics (Table A-2), described respectively in Sections 3 and 4 are presented here. The measurement uncertainties are reported at the k = 2, 95 % confidence interval. Note that Table A-1 spans 3 pages, intended to be laid out in a horizontal sequence. The tests are listed in order of increasing ELT (RTD 3604), starting with the ‘minimum’ test with ELT 10 °C, and ending with the ‘maximum’ test with ELT 39 °C.

Table A-1: Raw measurements for the CO_2 GSAC (continued on next 2 pages)

Test[1]	Date	Time	ID#	Dew 3504	Dew 3506	DP 3318	DP 3319	DP 3320	DP 3322	D 1500	D 3502	MF 1400	MF 3402	P 1200	P 1201	P 1202	P 1203	P 1204
				°C	°C	kPa	Pa	Pa	Pa	kg/m^3	kg/m^3	g/s	g/s	kPa	kPa	kPa	kPa	kPa
	yyyy-mm-dd	hh:mm:ss		±0.25	±0.25	±0.1	±2	±2	±2	±20	±0.5	±0.25 %	±0.25 %	±20	±20	±20	±20	±20
Min	2019-04-08	09:49:46	88	10.89	6.90	16.83	58.3	472.9	43.7	874	970.1	35.84	274.4	5504	5448	5449	5440	5402
ELT-1	2019-04-09	14:00:28	93	14.69	11.14	16.66	58.6	477.0	45.6	853	969.2	42.96	275.0	5544	5476	5478	5471	5445
ELT-2	2019-04-08	14:43:12	90	14.62	11.37	18.37	59.0	456.7	46.6	843	966.9	40.94	273.6	6130	6064	6068	6063	6036
Part Load	2019-04-09	12:16:59	92	14.67	12.28	19.46	58.6	474.5	45.6	822	963.9	39.08	272.7	6746	6693	6698	6694	6668
Standard	2019-04-05	10:54:54	87	14.39	12.40	20.11	59.1	460.6	43.9	806	961.0	37.40	272.3	7368	7313	7321	7315	7288
Standard	2019-04-10	14:51:47	96	14.45	12.43	20.84	59.6	454.1	47.8	804	961.2	37.20	271.7	7354	7304	7310	7303	7288
ELT-3	2019-04-10	12:05:26	95	14.38	13.01	22.34	56.9	451.3	45.1	788	958.1	35.72	271.5	8202	8156	8161	8150	8137
ELT-4	2019-04-08	12:33:33	89	14.51	13.44	22.78	56.5	455.2	43.6	780	954.8	33.77	270.5	9363	9328	9332	9323	9317
ELT-5	2019-04-09	09:28:52	91	14.38	13.51	22.96	58.6	452.7	46.3	782	953.4	32.91	269.8	9844	9801	9817	9801	9761
Max	2019-04-10	10:08:42	94	18.98	17.96	23.94	58.0	449.1	47.0	738	951.6	39.01	268.3	9792	9752	9755	9744	9742

[1]Datafile name: CO2-GSAC-Test-Data_Rev-3_9_4.EES

Note: All uncertainties are for k = 2 (95 % confidence interval)

Table A-1 (cont.)

Test[1]	P 1205	P 1206	P 1207	P 1216	P 1217	P 1218	P 3317	RTD 1600	RTD 1601	RTD 3602	RTD 3603	**RTD[2] 3604**	RTD 3607	RTD 3700	RTD 3701	RTD 3702	RTD 3703	RTD 3704
	kPa ±20	kPa ±20	kPa ±20	kPa ±20	kPa ±1	kPa ±1	kPa ±1	°C ±0.075	°C ±0.075	°C ±0.075	°C ±0.075	**°C ±0.075**	°C ±0.075	°C ±0.075	°C ±0.075	°C ±0.075	°C ±0.075	°C ±0.075
Min	3909	3882	3891	3888	321.0	313.9	300	10.08	17.40	17.43	9.21	**9.97**	8.67	21.01	21.16	21.10	8.48	8.44
ELT-1	4327	4288	4287	4278	308.8	301.9	288	10.11	18.31	18.35	9.33	**9.99**	12.96	27.00	26.85	26.93	12.74	12.70
ELT-2	4399	4358	4357	4348	332.0	325.3	310	15.08	22.86	22.90	14.12	**14.96**	13.35	26.86	26.85	26.89	13.12	13.08
Part Load	4500	4462	4458	4450	347.6	341.0	324	20.10	27.44	27.47	19.06	**20.00**	14.26	27.06	27.23	27.22	14.06	14.01
Standard	4574	4535	4534	4525	372.0	365.5	348	25.10	31.99	32.01	23.95	**25.01**	14.63	26.89	27.06	27.07	14.41	14.36
Standard	4564	4523	4519	4511	355.7	349.3	331	25.09	31.97	32.00	24.57	**25.00**	14.59	26.84	27.13	27.07	14.36	14.31
ELT-3	4664	4620	4617	4609	368.3	361.9	342	30.05	36.54	36.57	29.78	**29.97**	15.17	26.93	27.34	27.25	14.97	14.91
ELT-4	4753	4718	4714	4706	386.1	379.9	359	35.06	41.27	41.29	34.45	**34.99**	15.77	26.77	27.22	27.15	15.61	15.55
ELT-5	4760	4723	4720	4713	384.9	378.6	358	36.85	42.95	42.98	36.74	**36.79**	15.78	26.66	27.18	27.09	15.60	15.54
Max	5302	5247	5236	5227	382.1	375.9	355	39.08	45.57	45.59	36.56	**39.01**	20.40	31.57	31.88	31.89	20.23	20.16

[1]Datafile name: CO2-GSAC-Test-Data_Rev-3_9_4.EES

[2]RTD 3604 measures the ELT

Note: All uncertainties are for k = 2 (95 % confidence interval)

Table A-1 (cont.)

Test[1]	RTD 3705	RTD 3706	RTD 3707	TC 1100	TC 1101	TC 1102	TC 1103	TC 1104	TC 1105	TC 1106	TC 1107	TC 1108	TC 1109	W 1304	W 1305	W 1306	W 3300
	°C ±0.075	°C ±0.075	°C ±0.075	°C ±0.6	°C ±0.6	°C ±0.6	°C ±0.6	°C ±0.6	°C ±0.6	°C ±0.6	°C ±0.6	°C ±0.6	°C ±0.6	W ±0.2 %	W ±0.2 %	W ±0.2 %	W ±0.2 %
Min	8.42	8.65	8.62	45.1	44.3	10.37	9.8	9.7	4.8	9.1	9.3	10.3	10.4	1102	137.1	103.5	759.9
ELT-1	12.70	12.94	12.91	37.3	36.6	10.96	12.5	12.4	8.6	13.1	13.3	11.4	11.5	995	137.3	105.2	634.7
ELT-2	13.07	13.33	13.30	48.6	47.9	15.52	14.5	14.3	9.3	13.5	13.7	15.3	15.4	1163	136.3	103.3	1005.1
Part Load	14.00	14.25	14.22	60.1	59.4	20.37	17.8	17.4	10.2	15.2	15.3	19.9	19.9	1323	134.0	103.9	1056.9
Standard	14.35	14.61	14.58	71.6	70.7	25.24	20.6	20.2	10.9	15.1	15.4	24.6	24.6	1471	132.2	98.4	1212.5
Standard	14.29	14.57	14.54	71.8	70.8	25.24	20.8	20.3	10.8	15.3	15.6	24.6	24.6	1466	132.9	103.6	299.5
ELT-3	14.90	15.15	15.12	85.4	84.2	30.13	24.0	23.3	11.7	15.8	16.1	29.5	29.5	1677	132.3	100.8	87.5
ELT-4	15.53	15.76	15.73	101.8	100.3	35.07	27.2	26.4	12.5	16.8	17.1	34.4	34.2	1945	130.6	98.5	506.2
ELT-5	15.52	15.76	15.73	108.3	106.5	36.79	28.1	27.2	12.6	16.7	17.1	36.1	35.9	2055	129.7	101.3	1.0
Max	20.13	20.38	20.36	99.2	98.2	39.04	32.1	31.2	16.9	21.3	21.6	38.3	38.1	1988	130.0	102.5	2909.5

[1]Datafile name: CO2-GSAC-Test-Data_Rev-3_9_4.EES

Note: All uncertainties are for k = 2 (95 % confidence interval)

Table A-2: Calculated performance metrics for the CO_2 GSAC

Test[1]	COP_{adj}	$\frac{COP_{LLSL}}{COP_{basic}}$	ε_{LLSL}	η_{com}	η_{v}	γ_{com}	P_1/P_{13}	$Q_{c,liq}$	$Q_{c,vap}$	$Q_{c,2ph}$	$Q_{c,SupCrit}$	Q_{lat}	$Q_{sens,adj}$	$Q_{total,adj}$	V_n
	W/W	--	--	--	--	--	--	W	W	W	W	W	W	W	L/s
	±4 %	N/A	Fig. 20	±0.01	±0.009	Fig. 18	±0.007	±100	±50	±60	±120	±200	±150	±275	±10
Min	5.98	0.999	0.902	0.443	0.861	0.091	1.416	863	1984	5846	0	2051	5480	7531	347
ELT-1	7.32	0.992	0.832	0.412	0.889	0.052	1.296	994	1845	6960	0	2317	6119	8436	352
ELT-2	6.00	0.985	0.871	0.468	0.868	0.083	1.410	1068	2546	5628	0	2077	5820	7897	343
Part Load	4.92	0.983	0.906	0.499	0.842	0.104	1.516	1194	3388	4093	0	1603	5639	7242	352
Standard	4.14	0.986	0.935	0.528	0.825	0.122	1.628	1708	4830	1576	0	1295	5395	6690	343
Standard	4.13	0.986	0.936	0.529	0.824	0.120	1.630	1650	4776	1655	0	1322	5337	6660	344
ELT-3	3.31	1.001	0.956	0.548	0.802	0.135	1.779	0	0	0	7622	909	5130	6038	343
ELT-4	2.66	1.021	0.962	0.559	0.768	0.149	1.990	0	0	0	7243	721	4835	5556	344
ELT-5	2.44	1.026	0.964	0.563	0.757	0.161	2.089	0	0	0	7126	585	4783	5368	345
Max	2.67	1.048	0.956	0.566	0.787	0.144	1.874	0	0	0	7492	872	4820	5692	345

[1]Datafile name: CO2-GSAC-Test-Data_Rev-3_9_4.EES